Article:
Selwood, M. P., Fittinghoff, D. N., Volegov, P. L. et al. (2 more authors) (2023) A coded aperture with sub-mean free-path thickness for neutron implosion geometry imaging on inertial confinement fusion and inertial fusion energy experiments. Review of Scientific Instruments. 113501. ISSN 0034-6748

https://doi.org/10.1063/5.0167426

A coded aperture with sub-mean-free-path thickness for neutron implosion geometry imaging on inertial confinement fusion and inertial fusion energy experiments

M. P. Selwood*

Lawrence Livermore National Laboratory, Livermore, California 94550, USA

York Plasma Institute, School of Physics Engineering and Technology, University of York, Heslington, York YO10 5DD, UK

D. N. Fittinghoff, P. L. Volegov, and G. J. Williams

Lawrence Livermore National Laboratory, Livermore, California 94550, USA

C. D. Murphy

York Plasma Institute, School of Physics Engineering and Technology, University of York, Heslington, York YO10 5DD, UK

(*selwood1@llnl.gov)

(Dated: October 14, 2023)

Abstract

Inertial confinement fusion and inertial fusion energy experiments diagnose the geometry of the fusion region through imaging of the neutrons released through fusion reactions. Pinhole arrays typically used for such imaging require thick substrates to obtain high contrast along with a small pinhole diameter to obtain high resolution capability, resulting in pinholes that have large aspect ratios. This leads to expensive pinhole arrays that have small solid angles and are difficult to align. Here, we propose a coded aperture with scatter and partial attenuation (CASPA) for fusion neutron imaging, that relaxes the thick substrate requirement for good image contrast. These coded apertures are expected to scale to larger solid angles and be easier to align without sacrificing imaging resolution or throughput.

We use Monte Carlo simulations (Geant4) to explore a coded aperture design to measure neutron implosion asymmetries on fusion experiments at the National Ignition Facility (NIF) and discuss the viability of this technique, matching the current nominal resolution of 10 m. The results show that a 10 mm thick tungsten CASPA can image NIF implosions with neutron yields above 10^{14} with quality comparable to unprocessed data from a current NIF neutron imaging aperture. This CASPA substrate is 20 times thinner than the current aperture arrays for fusion neutron imaging, and less than one mean-free-path of 14.1 MeV neutrons through the substrate. Since resolution, solid angle and throughput are decoupled in coded aperture imaging, the resolution and solid angle achievable with future designs will be limited primarily by manufacturing capability.

I. INTRODUCTION

Inertial confinement fusion (ICF) and inertial fusion energy (IFE) schemes use heating and compression of a small-diameter deuterium-tritium (DT) fuel capsule to instigate fusion reactions and produce 14.1 MeV neutrons[1, 2]. The imaging of these neutrons is used to diagnose the shape and size of the fusion region within the fuel. With the fuel being relatively small (100 m to 10 mm[3, 4]), it requires 10-100 m imaging resolution to resolve undesirable features in the shape of the fusion region that may result in reduced neutron yields.

ICF neutron imaging is typically performed with a pinhole aperture of high aspect ratio. The pinhole diameter needs to be small to produce the imaging resolution required, while the substrate needs to be thick to create imaging contrast as the mean free path of fast fusion neutrons through materials is long. For example, a neutron imaging aperture at the National Ignition Facility (NIF)

has a 20 cm thick gold substrate and a minimum pinhole diameter of 5 m[5], with a 14.1 MeV neutron mean free path of 3.2 cm. The manufacture of a NIF neutron aperture is non-trivial and expensive, computationally heavy reconstruction is required to analyse the data, and the solid angle is small - with the ramification of low alignment tolerance. It is noted that penumbral techniques[6, 7] are used for imaging lower neutron yields ($\lessapprox 10^{13}$) due to their higher throughput, but they have a lower resolution capability with respect to the pinhole arrays[8] and so have not been included in this discussion.

Coded apertures have some advantages over single pinholes or pinhole arrays that are relevant for ICF and IFE. The decoupling of throughput and resolution allows for large coded apertures with larger solid angles to be created without sacrificing imaging resolution[9], and near-50% throughput is advantageous in low yield systems[10]. Recent work in x-ray imaging has shown that a coded aperture with scatter and partial attenuation (CASPA) can allow for thinner substrates to be used without detriment to the contrast of the reconstructed image[11]. Here, we discuss the application of thinner coded apertures to image neutrons produced in ICF sources where attenuation effects are negligible, simulating a CASPA compatible with the NIF and compare it with current aperture capability. We discuss the procedure for designing the aperture, including substrate material and thickness, and highlight how the design is unique for not only the incident neutron energy, but also source and diagnostic geometry.

Symmetric (or well characterised) implosion geometry is also key for IFE schemes. Like ICF, the neutron yield is dependent on source geometry, and in order to maximise net energy gain the fuel burn geometry must be diagnosed and monitored. Due to the similarity in requirements to ICF neutron imaging, the work discussed here for a NIF-like imaging system is also IFE relevant, allowing for new diagnostics to be designed into IFE plant concepts with a larger imaging solid angle and better alignment tolerances.

II. CODED APERTURES WITH SCATTER AND PARTIAL ATTENUATION

Coded apertures are a type of multi-pinhole array where individual projections of the source overlap on the detector and undergo reconstruction in post-processing to form a likeness of the source[12]. The signal on the detector, $\boldsymbol{D}$, akin to single pinhole imaging apertures, is the convolution of the source, $\boldsymbol{S}$, with the aperture design, $\boldsymbol{A}$;

$$\boldsymbol{D}(k,l) = \sum_{i,j} \boldsymbol{S}(i,j) \cdot \boldsymbol{A}(k-i, l-j) \tag{1}$$

where $\boldsymbol{D}$ is known as a *hologram* due to its lack of visible similarity to the source. (i,j) are 2D coordinates on the source plane, and (k,l) are 2D coordinates on the detector plane. A discreet representation of (i,j) and (k,l) on a regular grid system has been used, corresponding to the pixelated detector signal on each plane and accounting for magnification. The encoding of the detector hologram in equation 1 is often expressed in literature through shorthand notation;

$$\boldsymbol{D} = \boldsymbol{S} * \boldsymbol{A} \tag{2}$$

The reconstructed image, $\hat{\boldsymbol{S}}$, is calculated with a cross-correlation of the hologram and some decoding function, $\boldsymbol{G}$[13];

$$\hat{\boldsymbol{S}}(i,j) = \sum_{k,l} \boldsymbol{D}(k,l) \cdot \boldsymbol{G}(i+k, j+l) \tag{3}$$

with shorthand notation of;

$$\hat{\boldsymbol{S}} = \boldsymbol{D} \star \boldsymbol{G} \tag{4}$$

By substitution of equation 2 into 4, the reconstructed image can be expressed as;

$$\hat{\boldsymbol{S}} = \boldsymbol{S} * (\boldsymbol{A} \star \boldsymbol{G}) \tag{5}$$

The decoding function is designed such that its cross-correlation with the aperture design produces a Dirac delta distribution;

$$\boldsymbol{A} \star \boldsymbol{G} = \delta \tag{6}$$

and then the reconstructed image is the same as the original source:

$$\begin{aligned} \hat{\boldsymbol{S}} &= \boldsymbol{S} * \delta \\ \hat{\boldsymbol{S}} &= \boldsymbol{S} \end{aligned} \tag{7}$$

When a background signal, $\boldsymbol{B}$, is introduced to equation 2:

$$\boldsymbol{D} = \boldsymbol{S} * \boldsymbol{A} + \boldsymbol{B} \tag{8}$$

the reconstruction of equation 4 becomes:

$$\begin{aligned} \hat{\boldsymbol{S}} &= (\boldsymbol{S} * \boldsymbol{A} + \boldsymbol{B}) \star \boldsymbol{G} \\ \hat{\boldsymbol{S}} &= \boldsymbol{S} + \boldsymbol{B} \star \boldsymbol{G} \end{aligned} \tag{9}$$

Therefore, if the background is uncorrelated with the aperture design (and therefore the decoding function) and the area is sufficiently large, the background variation will be averaged out in the unimodular decoding function and will be removed from the reconstructed image. This is discussed and simulated in more detail within Selwood *et al.*[11], and demonstrated in derivative work[14]. Here, the modified uniformly redundant array (MURA) is used for aperture pattern generation[13] which is generated from a prime number base, p, assuming an oversampled system[10].

III. EXPERIMENTAL CONSTRAINTS

Currently, neutron imaging on NIF is performed on 3 lines of sight with a neutron imaging aperture of multiple pinholes. Each individual pinhole projects the source onto a scintillator, which is imaged by a time-gated intensified charge coupled device (CCD). Each line of sight has a different neutron imaging aperture installed, and here the aperture from neutron imaging system 1 (NIS1) will be used to compare with the CASPA. This neutron imaging aperture and scintillator are 32.5 cm and 28 m from the source respectively, with 20 triangular and 3 penumbral pinholes. An image of this aperture can be seen in figure 1a. The substrate is 20 cm thick gold[15], with the triangular pinholes tapered from 5 m closest to the source out to 226 m facing the detector[16]. This is to increase the solid angle of each individual pinhole without compromising the resolution capability[17] of 10 m[5].

A pre-existing line of sight on the NIF has been used to design the CASPA with a square detector 11.5 m from the source, as this would be the most likely location any new aperture tests would be performed without disrupting current neutron imaging capabilities. The detector modelled is akin to imaging plate detectors commonly fielded on this line of sight, using a plastic convertor to generate more readily detectable protons from incident neutrons. Its area is 2 inches square, in

order to keep the number of incident neutrons and detector solid angle comparable with the aforementioned time-gates CCDs to allow qualitative comparisons of the synthetic and experimental data. For 14.1 MeV neutrons, 2 mm of high-density plastic is the optimal convertor[18, 19], and MS or TR imaging plate for detection. This evaluation models the combined detector, of convertor and imaging plate, to be 10% quantum efficient with a resolution of 500 m, as an estimate to combine multiple signal loss and blur contributions processes.

Design Parameters		**Calculated Aperture Parameters**	
Detector Area	2×2 inches	**MURA *p* value**	97
Detector Pixel Size	500×500 m	**Aperture Element Size**	10×10 m
Detector Stand-off	11.5 m	**Aperture Stand-off**	11.5 cm
Resolution Capability	10 m		

TABLE I: An example of candidate CASPA parameters for use at the NIF, calculated from existing detector information and desired resolution capability.

With a known detector area, pixel size, and resolution requirement to match the capability of current neutron imaging system, the CASPA parameters can be calculated[20, 21]. The parameters can be seen in table I and a visual comparison between the NIF aperture and CASPA is shown in figure 1. The CASPA imaging system has a solid angle of 37 sr, compared to 3 sr of NIS1 on the NIF and 0.38 sr for an individual pinhole on the neutron imaging aperture. Therefore, all 20 pinholes of the NIF aperture do not completely overlap in field of view, and thus cannot all give clear images of the source simultaneously. Coded apertures make more efficient use of detector area, and if detector area increases the CASPA solid angle and total signal will be able to increase more rapidly than the NIF aperture array.

Note that this CASPA is only designed to match the current resolution capability of NIS1. If a CASPA could be manufactured with smaller element sizes, the inherent decoupling of resolution and throughput of coded apertures means it is possible for the CASPA to better the current resolution capability of the NIF aperture without loss of signal level or solid angle.

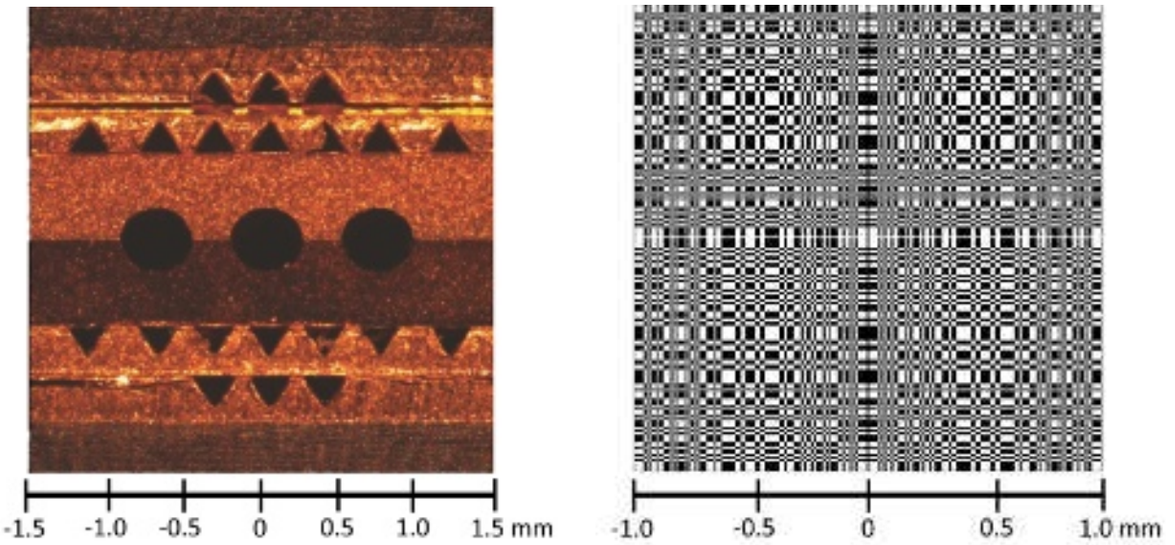

(a) (b)

FIG. 1: A comparison of the back surface (detector facing) of (a) the NIF neutron imaging aperture on NIS1[5] and (b) the proposed *p*97 CASPA. The three large holes in the central row of (a) are for penumbral imaging, and the white and black regions on (b) are pinhole and substrate, respectively. (a) reproduced from Merrill *et. al.*, Rev. Sci. Instrum. **83** (2012), with the permission of AIP Publishing

IV. SUBSTRATE MATERIAL

Commonly used high-Z and machinable materials of gold, tungsten, and platinum have been evaluated for substrate performance. Table II shows that scatter will be the primary mechanism for generating hologram contrast for neutron imaging, as the attenuation probabilities are orders of magnitude lower. For a coded aperture with sub-mean-free path thickness, it is unlikely that the neutron will interact more than once with the substrate, and thus it is also unlikely a down-scattered neutron would be attenuated. This differs from the original x-ray study where attenuation was a prevalent mechanism[11], but the name CASPA has been kept for consistency.

Per unit length of material, gold has the highest probability of scattering the incident neutron. However, table II does not indicate the neutron scattering angle. For a small scatter angle, the neutron may still be detected on the same detector pixel, rendering the scatter unresolvable. Therefore the probability of scatter alone cannot be used to decide CASPA substrate material.

To quantify a materials performance as a CASPA substrate, Monte Carlo simulations were run

Substrate	Scatter $_{\text{elastic}}$ (/cm)	Scatter $_{\text{inelastic}}$ (/cm)	Attenuation (/cm)
Tungsten-182	0.166±0.006	0.032±0.006	$(6\pm6)\times10^{-5}$
Platinum-194	0.15±0.01	0.02±0.01	$(6\pm6)\times10^{-5}$
Gold-197	0.174	0.036	6.6×10^{-5}

TABLE II: The probability of interaction per unit length for approximately DT fusion neutron energies incident on various substrates in their most abundant isotopes. Calculated as the inverse of mean free path[22, 23].

to simulate the proportion of particles that are either attenuated or undergo sufficient scattering reaction(s) within the substrate bulk to be perturbed away from the inline pixel on the detector. The furtive[24]-direct ratio is the number of scattered or attenuated neutrons for every unperturbed neutron passing through the material:

$$\text{FDR} = \frac{\Gamma - \lambda}{\lambda} \tag{10}$$

where Γ is the total number of DT neutrons initialised during the simulation, and λ is the total signal neither scattered nor attenuated by the material. λ is recorded on a 500×500 m detector, 11.385 m from the material, which corresponds to a single pixel of the detector from table I. Hence it is possible for scattered neutrons to still contribute to λ, if the detector would be unable to resolve the small angle of scatter, and as such the FDR may differ from the mean free path and vary with experimental setup.

Figure 2 shows platinum is the most effective CASPA substrate, but with $< 1\%$ improvement over tungsten. For higher substrate thicknesses, using a gold substrate may require a 1-2 mm thicker CASPA than with a platinum substrate to achieve similar performance. Due to the large difference in raw material cost and comparable performance, tungsten is used as the substrate of choice for this study.

V. SUBSTRATE THICKNESS

The minimum substrate thickness of a CASPA is the thinnest for which the source is effectively imaged. This is difficult to quantify, as effective source imaging is subjective and dependent on

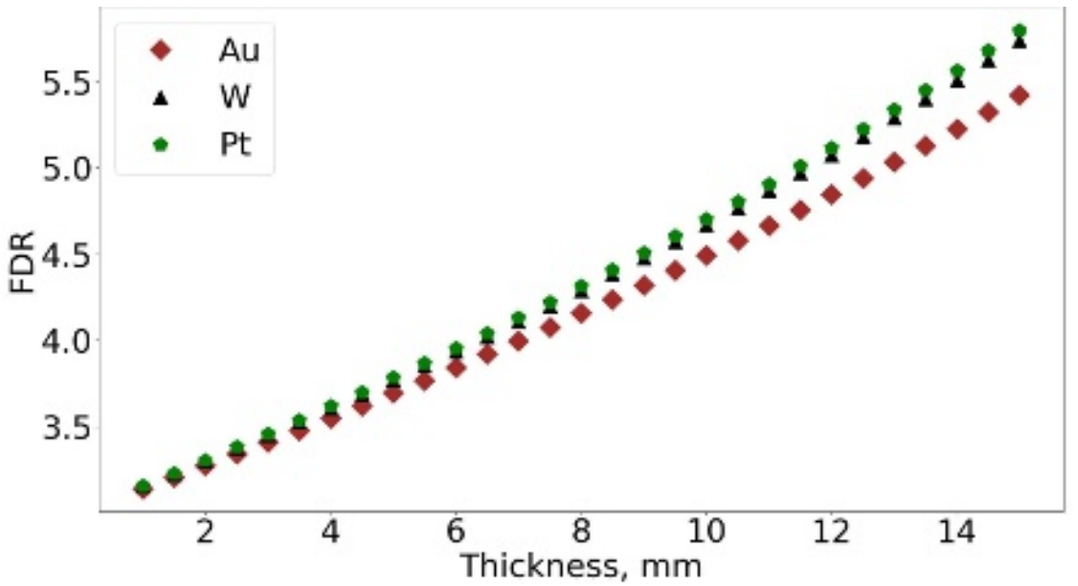

FIG. 2: A comparison between the FDR of tungsten, platinum, and gold substrates with DT fusion neutrons. Tungsten has the greatest attenuation cross-section, gold has the better scattering cross-section, with platinum between each extreme.

the outcome required, as well as the incident particle energy, source geometry and flux. Here, effective source imaging is defined as the ability to reconstruct a known Gaussian source to the correct diameter with a χ^2 below the critical value of 1. Legendre modes at the 17% contour have been used for Gaussian creation and analysis[25], with a P_0 of 40 m chosen to replicate a typical NIF-like implosion radius.

Note that there is only a minimum aperture thickness required, and no theoretical maximum. The CASPA should be designed for the highest incident energy neutron anticipated, and everything below that energy will still be imaged effectively due to the higher attenuation and scatter cross-sections for the lower energy particles. Exceptions may arise around transmission peaks of the substrate material and prevalence of $(2, 2n)$ and higher-order multi-neutron producing reactions, but this will be unique to individual experiments, where alternative materials may be preferable for a CASPA substrate.

For fusion neutrons, the tungsten thickness required for the CASPA is evaluated using a simulated mono-energetic 14.1 MeV neutron source. The measurable neutron yield on NIF is between 10^{10} and 10^{19} across 4π radially from the capsule implosion[26], with yields of 10^{14} - 10^{15} being average for previous DT shots[27], dictating the minimum yield range over which the CASPA

would be expected to perform. The CASPA designed would also effectively image the current published record of 4.8×10^{17} neutrons on N210808[28] and target gain achieved on N221204[29].

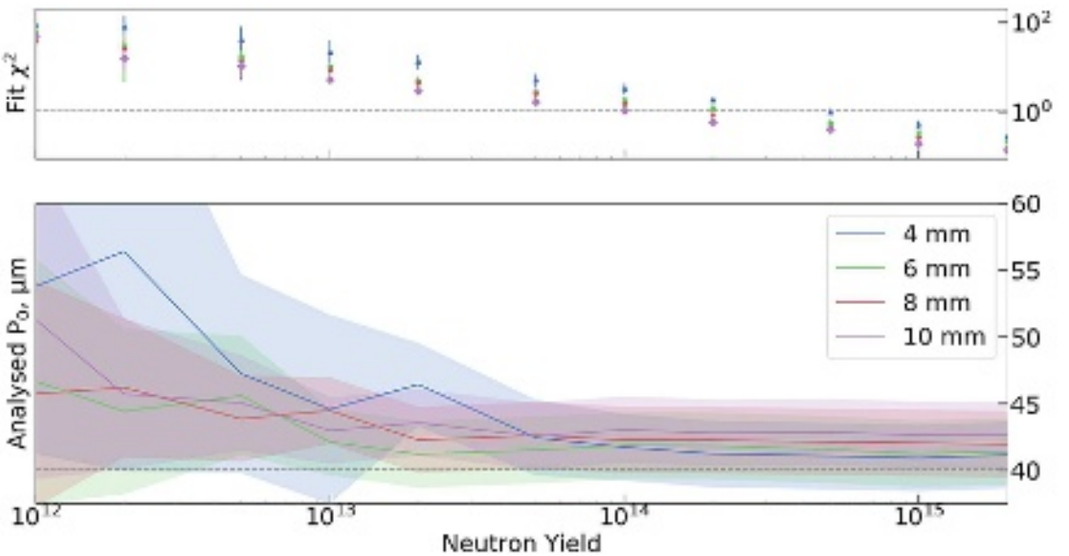

FIG. 3: Benchmarking CASPA effectiveness at 4 different thicknesses for accurately imaging a $P_0 = 40$ m Gaussian source as a function of neutron yield. χ^2 is from Legendre mode fitting, and error bars are either the standard deviation of 5 repeats or the diagnostic resolution, whichever is greater.

A dataset of individual Geant4 simulations have been plotted in figure 3 for 4 different tungsten CASPA thicknesses, looking at the variation of analysed P_0 as a function of total neutron yield. As the source is a known, symmetric Gaussian, the analysis was constrained such that $P_n = 0$ for $n > 0$. It can be seen that a 10 mm W CASPA has a χ^2 below the critical value of 1, and a P_0 of 43 ± 3 m, fulfilling the requirement for effective source imaging.

VI. COMPENSATING FOR COLLIMATOR EFFECTS

The $P_0 = 43 \pm 3$ m for the 10 mm W CASPA only narrowly encompasses the input P_0 of 40 m despite the χ^2 below the critical value. A trend is apparent across the four aperture thicknesses shown in figure 3, with the thinner apertures converging closer to the input parameters than their thicker counterparts. This is highlighted further in figure 5, showing the percentage difference between analysed and initial P_0 for different aperture thicknesses and source sizes. It can be seen that there are correlations with both parameters, and as such further correction factors, iterative

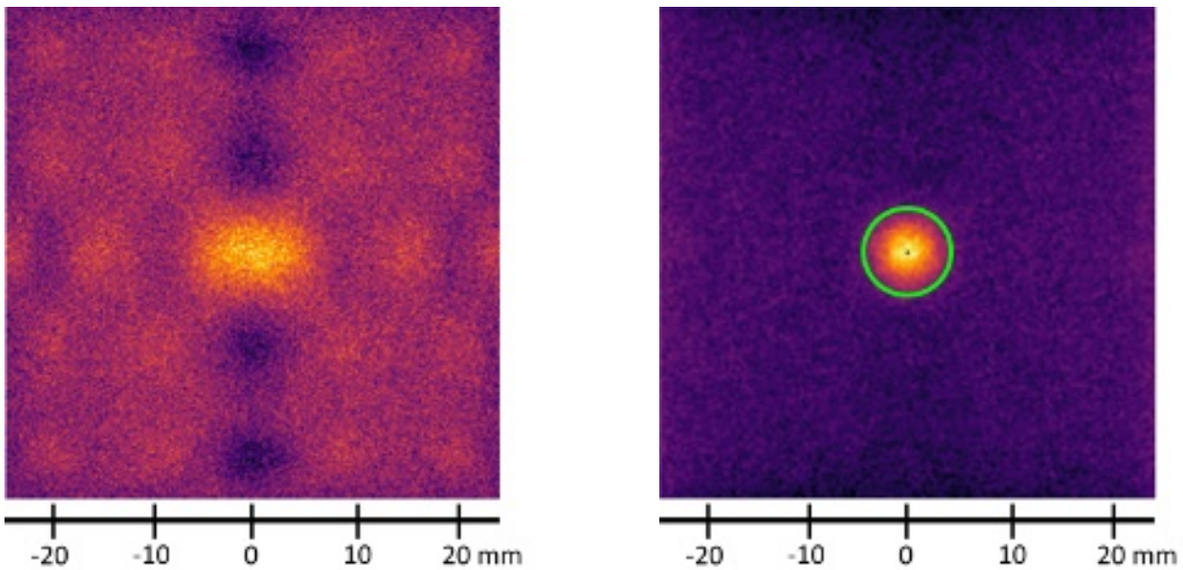

(a) (b)

FIG. 4: a) A synthetic hologram from a P_0 of 40 m 10^{14} yield NIF-like neutron source and (b) its reconstructed source image with $\chi^2 \leq 1$ and a $P_0 = 43 \pm 3$ m shown in green.

reconstruction methods, or both should be applied to create a cleaner decode with less background artefact generation.

Such errors arise from a decoding function that does not relate well enough with the aperture design due to collimator effects of thick aperture imaging. In essence, the 2D aperture design is not representative of the 3D aperture's point spread function upon the detector. The dependency on source size and aperture thickness would suggest an error increasing when the angle of incidence between the particle and the aperture increases. Neutrons with a greater angle of incidence upon the aperture will have a longer path length through the substrate, resulting in a lower signal count on the detector than expected by the decoding function.

Mask / anti-mask imaging can be used to increase decoding accuracy of coded apertures, by removing any possible aperture throughput bias and by integrating over 2 or more decoded images[30]. However, single-shot experiments such as the NIF do not have the luxury of identical repeat shots for which the aperture can be rotated. Here, the aperture design bias is approximated for single-shot experiments by a function of the form:

$$C(\phi, n) = \cos(n\phi) \tag{11}$$

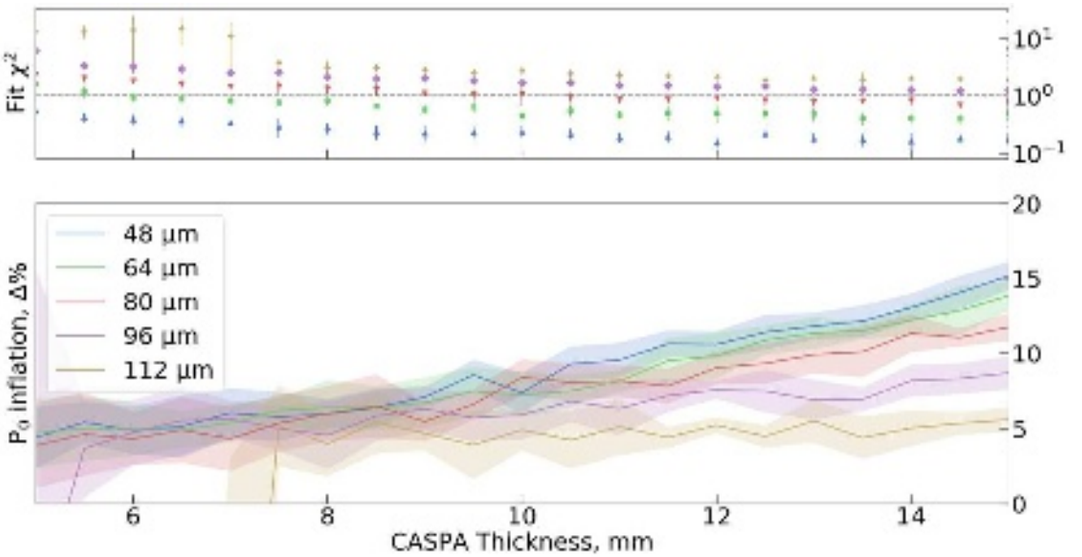

FIG. 5: The error in P_0 measurement from a known source diameter, as a function of aperture thickness. Results all use a consistent neutron yield of 10^{14}. For large P_0 and thinner aperture, the Gaussian was too degraded to adequately analyse. χ^2 is from Legendre mode fitting, and error bars are the standard deviation of 5 repeats.

where ϕ is the angle subtended from the central axis of the source place to the detector pixel, and the multiplier n will be a function of aperture thickness and source size. The role of this correction factor upon the hologram is to reduce the variation in background back to a quasi-uniform plane, which results in a constant background across the reconstructed image. The standard deviation of $\hat{\boldsymbol{S}}$ is used as the figure of merit to analyse the effect of $C(n)$ on decoded image background levels, which can be seen in figure 6. By finding the minimum of the graph, a suitable n can be found empirically for an individual hologram – for the reconstructed image of figure 7f, $n_{\text{optimum}} = 36.8$. The reduction in background can be seen in figure 6. The analysed P_0 and χ^2 changed from 43 ± 3 m and 1.00 pre-correction to 41 ± 3 m and 0.87 post-correction.

VII. COMPARISON WITH THE NIF

Figure 3 suggests that a 10 mm W CASPA can deliver effective source imaging akin to that achieved with a 20 cm Au pinhole array currently used on the NIF. This is a 20× reduction in aperture thickness alongside the previously discussed order of magnitude increase in solid angle. Figure 7 shows an example of a hologram generated from a single simulation of a 10^{14} neutron

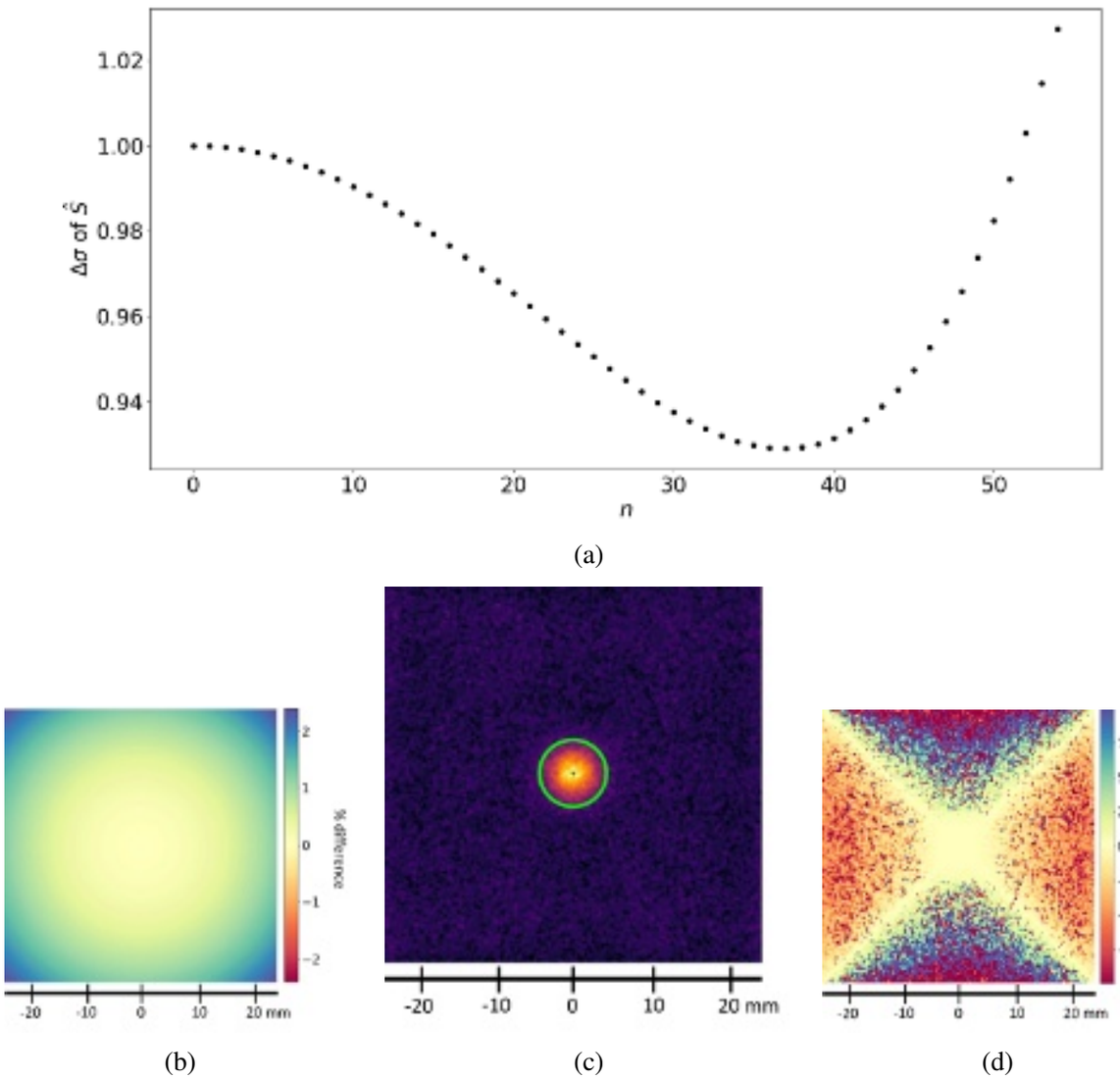

(a)

(b) (c) (d)

FIG. 6: (a) The variation in standard deviation across the reconstructed image as a function of n, where equation 11 is applied to the hologram pre-decoding. The minimum of the function, $n = 36.8$, had been applied to the hologram of figure 7e, and (b) the percentage difference between the two holograms shown. The hologram of (b) is decoded to produce (c) the source reconstruction. (d) is the percentage difference between (c) and the original reconstruction in figure 7f. (c) has an analysed P_0 of 41 ± 3 m shown in green, in comparison to (figure 7f) 43 ± 3 m.

yield, after the collimator effect correction from equation 11. The reconstructed image shows the Gaussian input with $P_0 = 41 \pm 3$ m with a χ^2 below the critical value of 0.87, and is displayed

against the raw data from the best single NIF pinhole image from an experiment of comparable yield but smaller source size of $P_0 = 22 \pm 3$ m[5]. Although noise is still present in the CASPA reconstruction which was not created by the source, a qualitative comparison with the NIF aperture shows similar levels of background variability.

The differences in aperture design requirements will change the manufacturing challenges for the CASPA with respect to a NIF aperture. Any fusion neutron apertures are too large, with too high an aspect ratio to machine from a solid block of metal. Instead, they must be made in smaller, more manageable sheets and assembled. These sheets can either be along the collimation axis, or perpendicular to it.

The NIF neutron imaging aperture of figure 7a is manufactured along the collimator axis. The triangular pinholes are etched as grooves, and then stacked atop a non-etched sheet to form the pinhole. This allows for fine control over taper features for the full length of the aperture, but limits the technique to pinholes on rowed grids. The separate sheets can be seen through discolouration in figure 7a. Having a defined metrology for the aperture is paramount for maximum likelihood reconstruction of the experimental images, which is a difficult task for such high aspect ratio tapered features.

The substantial reduction in aperture thickness for the CASPA reduces the collimator effect, and each individual pinhole has a larger solid angle without the need to taper. Furthermore, due to the highly transmissive nature of the substrate, the pinhole features can still be projected to the detector even when the solid angle of individual pinholes would not classically include the source. Having a non-tapered design allows for stacks perpendicular to the collimation axis to be used, made up of identical sheets extruded to the full aperture thickness. Highly intricate 2D micro-machining is more common than 3D, and thus the CASPA may be cheaper to manufacture than the NIF neutron imaging aperture in labour, while the thinner substrate would reduce the cost of raw materials.

VIII. NEED FOR ITERATIVE RECONSTRUCTION METHODS

Figure 7f shows a fluctuating background is still present across the CASPA image, and that the imaged source is not the perfect Gaussian input from the simulation. This is indicative of a point spread function that changes with position in the source plane. this is not accounted for in the definition of $\boldsymbol{G}$ in equation 4, and is caused by further collimator effects that equation 11 cannot

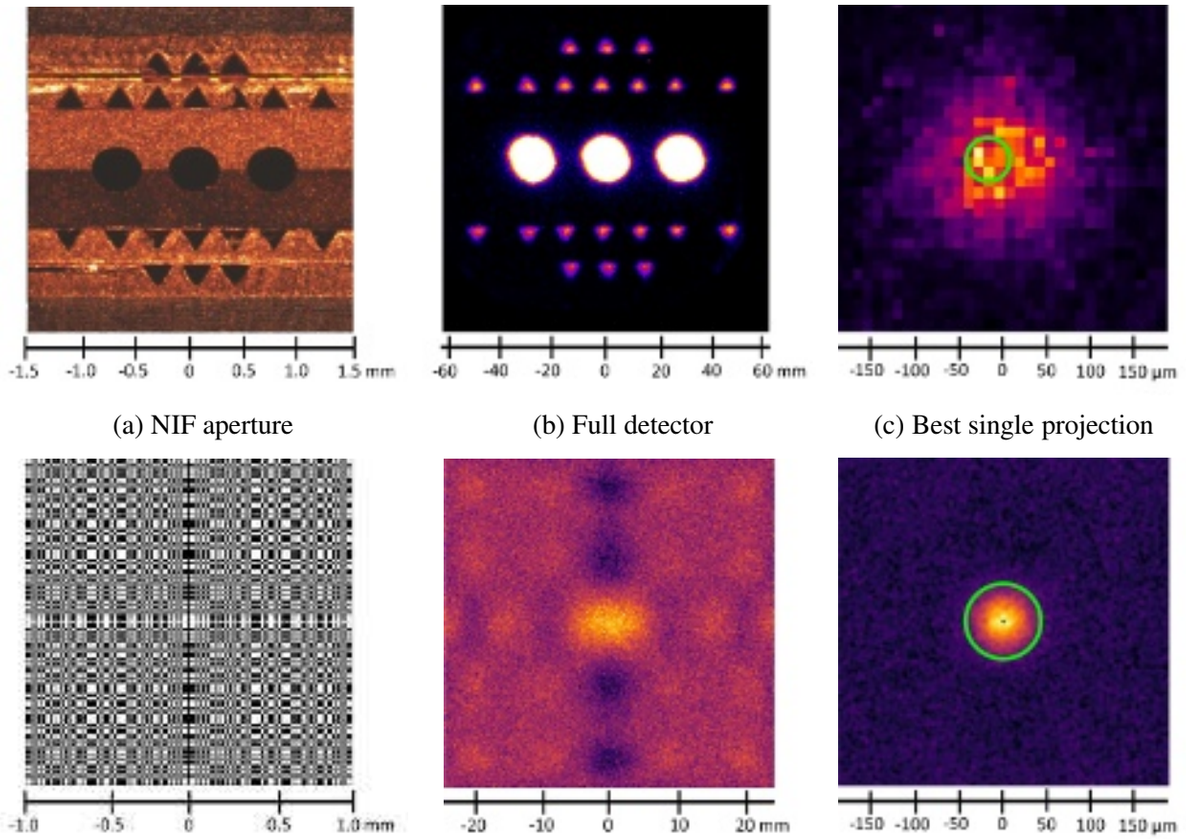

(a) NIF aperture (b) Full detector (c) Best single projection

(d) Simulated CASPA (e) CASPA hologram (f) Reconstructed projection

FIG. 7: (a) aperture, (b) image through all 20 tapered and 3 penumbral pinholes (with long-range blur and background subtraction applied) and (c) the best single pinhole from NIF shot N120412-001[5] scaled to the source plane. After the application of iterative reconstruction techniques[16], the source size was analysed as $P_0 = 22 \pm 3$ m[5], which has been overlaid in green. This is compared with (d) CASPA, (e) hologram and (f) reconstructed image from a simulated P_0 = 40 m simulation at comparable neutron yields, also scaled to the source plane. The $P_0 = 41 \pm 3$ m Legendre mode fit is shown in green. The raw data quality of (c) can be qualitatively compared to (f), with both possessing noise and background which would require iterative reconstruction techniques to remove[16]. (a)–(c) reproduced from Merrill *et. al.*, Rev. Sci. Instrum. **83** (2012), with the permission of AIP Publishing.

correct for.

However, a similar discrepancy can be seen in figure 7c, with a large background and fluctuation in the projection that outgrows the analysed P_0. The analysis routinely applied to data from the NIF

is an iterative reconstruction technique such as maximum likelihood expectation maximisation[16] or generalised expectation maximisation[31], which is used to reconstruct the most likely source geometry that would generate the detected projection. It is only through such techniques that the $P_0 = 22 \pm 3$ m cited is able to be determined[5]. These techniques could also be applied to CASPA holograms to reduce the background and improve reconstructed image quality in order to compare quantitatively with reconstructed images from experiments on the NIF. However, due to non-zero backgrounds and low contrast across the hologram, further research is required into the application of these techniques to a CASPA, as current coded aperture maximum likelihood expectation maximisation models are unsuitable[32, 33].

IX. CONCLUSION

In conclusion, coded apertures with scatter and partial attenuation could be used for ICF and IFE neutron imaging to allow for a higher solid angle imaging system without sacrificing resolution or throughput. With advances in manufacturing techniques, they may be able to move beyond the resolution capability of high-contrast pinhole imagers currently used on experiments such as the NIF. This is shown through simulation, suggesting that a 10 mm thick tungsten CASPA would be suitable for imaging DT fusion neutrons on the NIF, with non-tapered features of 10 m and a basic MURA pattern of $p97$ matching the current imaging resolution. This is a twenty-fold decrease in thickness with respect to the 20 cm thick neutron imaging aperture currently used, and a ten-fold increase in solid angle without detector changes.

Expectation maximisation reconstruction techniques are briefly discussed but not been applied here, which are used on NIF neutron data[16]. Using such iterative techniques, it is possible that a CASPA thinner than 10 mm could be fielded for neutrons yields of 10^{14}, or that the 10 mm aperture could be used to image lower source yields than shown. Further research is required into the application of expectation maximisation to data with non-zero backgrounds and low contrast before such iterative reconstruction techniques can be applied to a CASPA.

ACKNOWLEDGMENTS

This work was supported by the Engineering and Physical Sciences Research Council [EP/L01663X/1], Scitech Precision, and the Science and Technology Facilities Council, as well as performed under

the auspices of the U.S. Department of Energy by Lawrence Livermore National Laboratory under Contract DE-AC52-07NA27344.

LLNL-JRNL-851417.

---

[1] R. S. Craxton, K. S. Anderson, T. R. Boehly, V. N. Goncharov, D. R. Harding, J. P. Knauer, R. L. McCrory, P. W. McKenty, D. D. Meyerhofer, J. F. Myatt, A. J. Schmitt, J. D. Sethian, R. W. Short, S. Skupsky, W. Theobald, W. L. Kruer, K. Tanaka, R. Betti, T. J. Collins, J. A. Delettrez, S. X. Hu, J. A. Marozas, A. V. Maximov, D. T. Michel, P. B. Radha, S. P. Regan, T. C. Sangster, W. Seka, A. A. Solodov, J. M. Soures, C. Stoeckl, and J. D. Zuegel, Direct-drive inertial confinement fusion: A review (2015).

[2] J. L. Kline, S. H. Batha, L. R. Benedetti, D. Bennett, S. Bhandarkar, L. F. Hopkins, J. Biener, M. M. Biener, R. Bionta, E. Bond, D. Bradley, T. Braun, D. A. Callahan, J. Caggiano, C. Cerjan, B. Cagadas, D. Clark, C. Castro, E. L. Dewald, T. Döppner, L. Divol, R. Dylla-Spears, M. Eckart, D. Edgell, M. Farrell, J. Field, D. N. Fittinghoff, M. G. Johnson, G. Grim, S. Haan, B. M. Haines, A. V. Hamza, E. P. Hartouni, R. Hatarik, K. Henderson, H. W. Herrmann, D. Hinkel, D. Ho, M. Hohenberger, D. Hoover, H. Huang, M. L. Hoppe, O. A. Hurricane, N. Izumi, S. Johnson, O. S. Jones, S. Khan, B. J. Kozioziemski, C. Kong, J. Kroll, G. A. Kyrala, S. Lepape, T. Ma, A. J. Mackinnon, A. G. Macphee, S. Maclaren, L. Masse, J. McNaney, N. B. Meezan, J. F. Merrill, J. L. Milovich, J. Moody, A. Nikroo, A. Pak, P. Patel, L. Peterson, E. Piceno, L. Pickworth, J. E. Ralph, N. Rice, H. F. Robey, J. S. Ross, J. R. Rygg, M. R. Sacks, J. Salmonson, D. Sayre, J. D. Sater, M. Schneider, M. Schoff, S. Sepke, R. Seugling, V. Smalyuk, B. Spears, M. Stadermann, W. Stoeffl, D. J. Strozzi, R. Tipton, C. Thomas, P. L. Volegov, C. Walters, M. Wang, C. Wilde, E. Woerner, C. Yeamans, S. A. Yi, B. Yoxall, A. B. Zylstra, J. Kilkenny, O. L. Landen, W. Hsing, and M. J. Edwards, Progress of indirect drive inertial confinement fusion in the united states, Nuclear Fusion **59**, 10.1088/1741-4326/ab1ecf (2019).

[3] D. N. Fittinghoff, N. Birge, and V. Geppert-Kleinrath, Neutron imaging of inertial confinement fusion implosions, Review of Scientific Instruments **94**, 021101 (2023).

[4] D. Yager-Elorriaga, M. Gomez, D. Ruiz, S. Slutz, A. Harvey-Thompson, C. Jennings, P. Knapp, P. Schmit, M. Weis, T. Awe, G. Chandler, M. Mangan, C. Myers, J. Fein, B. Galloway, M. Geissel, M. Glinsky, S. Hansen, E. Harding, D. Lamppa, W. Lewis, P. Rambo, G. Robertson, M. Savage, G. Shipley, I. Smith, J. Schwarz, D. Ampleford, K. Beckwith, K. Peterson, J. Porter, G. Rochau, and

D. Sinars, An overview of magneto-inertial fusion on the z machine at sandia national laboratories, Nuclear Fusion **62**, 042015 (2022).

[5] F. E. Merrill, D. Bower, R. Buckles, D. D. Clark, C. R. Danly, O. B. Drury, J. M. Dzenitis, V. E. Fatherley, D. N. Fittinghoff, R. Gallegos, G. P. Grim, N. Guler, E. N. Loomis, S. Lutz, R. M. Malone, D. D. Martinson, D. Mares, D. J. Morley, G. L. Morgan, J. A. Oertel, I. L. Tregillis, P. L. Volegov, P. B. Weiss, C. H. Wilde, and D. C. Wilson, The neutron imaging diagnostic at NIF (invited), Rev. Sci. Instrum. **83**, 10.1063/1.4739242 (2012).

[6] L. Disdier, A. Rouyer, I. Lantuéjoul, O. Landoas, J. L. Bourgade, T. C. Sangster, V. Y. Glebov, and R. A. Lerche, Inertial confinement fusion neutron imagesa), Physics of Plasmas **13**, 056317 (2006).

[7] B. Bachmann, T. Hilsabeck, J. Field, N. Masters, C. Reed, T. Pardini, J. R. Rygg, N. Alexander, L. R. Benedetti, T. Döppner, A. Forsman, N. Izumi, S. LePape, T. Ma, A. G. MacPhee, S. Nagel, P. Patel, B. Spears, and O. L. Landen, Resolving hot spot microstructure using x-ray penumbral imaging (invited), Review of Scientific Instruments **87**, 11E201 (2016).

[8] V. E. Fatherley, D. N. Fittinghoff, V. Geppert-Kleinrath, G. P. Grim, H. J. Jorgenson, J. A. Oertel, D. W. Schmidt, P. L. Volegov, and C. Wilde, Evolution of the neutron imaging aperture, in *Radiation Detectors in Medicine, Industry, and National Security XIX*, Vol. 10763, edited by G. P. Grim, L. R. Furenlid, H. B. Barber, and J. A. Koch, International Society for Optics and Photonics (SPIE, 2018) pp. 167 – 175.

[9] M. J. Cieślak, K. A. Gamage, and R. Glover, Coded-aperture imaging systems: Past, present and future development – a review, Radiation Measurements **92**, 59 (2016).

[10] E. E. Fenimore and T. M. Cannon, Coded aperture imaging with uniformly redundant arrays, Applied Optics **17**, 337 (1978).

[11] M. P. Selwood, C. I. D. Underwood, R. Heathcote, and C. D. Murphy, Coded apertures with scatter and partial attenuation for high-energy high-resolution imaging, Plasma Physics and Controlled Fusion **62**, 10.1088/1361-6587/ab8ca4 (2020).

[12] E. E. Fenimore and T. M. Cannon, Uniformly redundant arrays: digital reconstruction methods, Appl. Opt. **20**, 1858 (1981).

[13] S. R. Gottesman and E. E. Fenimore, New family of binary arrays for coded aperture imaging, Applied Optics **28**, 4344 (1989).

[14] G. R. Davis, T. Beckenbach, and P. Meyer, Imaging a microfocus x-ray focal spot with a thin coded aperture, Scientific Reports **12**, 10.1038/s41598-022-23338-y (2022).

[15] M. D. Wilke, S. H. Batha, P. A. Bradley, R. D. Day, D. D. Clark, V. E. Fatherley, J. P. Finch, R. A. Gallegos, F. P. Garcia, G. P. Grim, S. A. Jaramillo, A. J. Montoya, M. J. Moran, G. L. Morgan, J. A. Oertel, T. A. Ortiz, J. R. Payton, P. Pazuchanics, D. W. Schmidt, A. C. Valdez, C. H. Wilde, and D. C. Wilson, The national ignition facility neutron imaging system, Review of Scientific Instruments **79**, 10E529 (2008).

[16] P. Volegov, C. R. Danly, D. N. Fittinghoff, G. P. Grim, N. Guler, N. Izumi, T. Ma, F. E. Merrill, A. L. Warrick, C. H. Wilde, and D. C. Wilson, Neutron source reconstruction from pinhole imaging at national ignition facility, Rev. Sci. Instrum. **85**, 10.1063/1.4865456 (2014).

[17] The number of resolvable features per unit length.

[18] T. Miura, M. Baba, T. Sanami, T. Yamazaki, M. Ibaraki, Y. Hirasawa, T. Hiroishi, T. Aoki, A. Yamadera, and T. Nakamura, Development of fast neutron profiling method, Nuclear Instruments and Methods in Physics Research Section A: Accelerators, Spectrometers, Detectors and Associated Equipment **476**, 337 (2002), int. Workshop on Neutron Field Spectrometry in Science, Technolog y and Radiation Protection.

[19] D. A. Sunnarborg, J. W. Peel, N. Mascarenhas, and W. Mengesha, Directional neutron detectors for use with 14 mev neutrons :fiber scintillation methods for directional neutron detection. (2005).

[20] M. P. Selwood, R. Heathcote, and C. D. Murphy, Imaging objects with coded apertures, utilising a laser wakefield x-ray source (Springer Proceedings in Physics Series., 2018).

[21] R. Heathcote, A. Anderson-Asubonteng, R. J. Clarke, M. P. Selwood, C. Spindloe, and N. Booth, Coded aperture x-ray imaging of high power laser-plasma interactions on the vulcan laser system (SPIE, 2018) p. 29.

[22] N. Soppera, M. Bossant, and E. Dupont, Janis 4: An improved version of the nea java-based nuclear data information system, Nuclear Data Sheets **120**, 294 (2014).

[23] CRC Handbook, *CRC Handbook of Chemistry and Physics*, 102nd ed. (CRC Press, 2021).

[24] The antithesis of direct.

[25] G. P. Grim and other, Nuclear imaging of the fuel assembly in ignition experiments, Phys. Plasmas **20**, 10.1063/1.4807291 (2013).

[26] G. W. Cooper and C. L. Ruiz, NIF total neutron yield diagnostic, Rev. Sci. Instrum. **72**, 814 (2001).

[27] A. L. Kritcher and other, Design of inertial fusion implosions reaching the burning plasma regime, Nat. Phys. **18**, 251 (2022).

[28] H. Abu-Shawareb *et al.* (Indirect Drive ICF Collaboration), Lawson criterion for ignition exceeded in

an inertial fusion experiment, Phys. Rev. Lett. **129**, 075001 (2022).

[29] DOE national laboratory makes history by achieving fusion ignition (2022).

[30] E. M. Brubaker, A maximum likelihood expectation maximization iterative image reconstruction technique for mask/anti-mask coded aperture data, in *2013 IEEE Nuclear Science Symposium and Medical Imaging Conference (2013 NSS/MIC)* (2013) pp. 1–3.

[31] P. L. Volegov, C. R. Danly, F. E. Merrill, R. Simpson, and C. H. Wilde, On three-dimensional reconstruction of a neutron/x-ray source from very few two-dimensional projections, Journal of Applied Physics **118**, 205903 (2015).

[32] Z. Mu and Y. H. Liu, Aperture collimation correction and maximum-likelihood image reconstruction for near-field coded aperture imaging of single photon emission computerized tomography, IEEE Trans. Med. Imaging **25**, 701 (2006).

[33] M. P. Selwood, *Coded Aperture Imaging: novel approaches to high-energy high-resolution laboratory imaging*, Ph.D. thesis, University of York (2022).

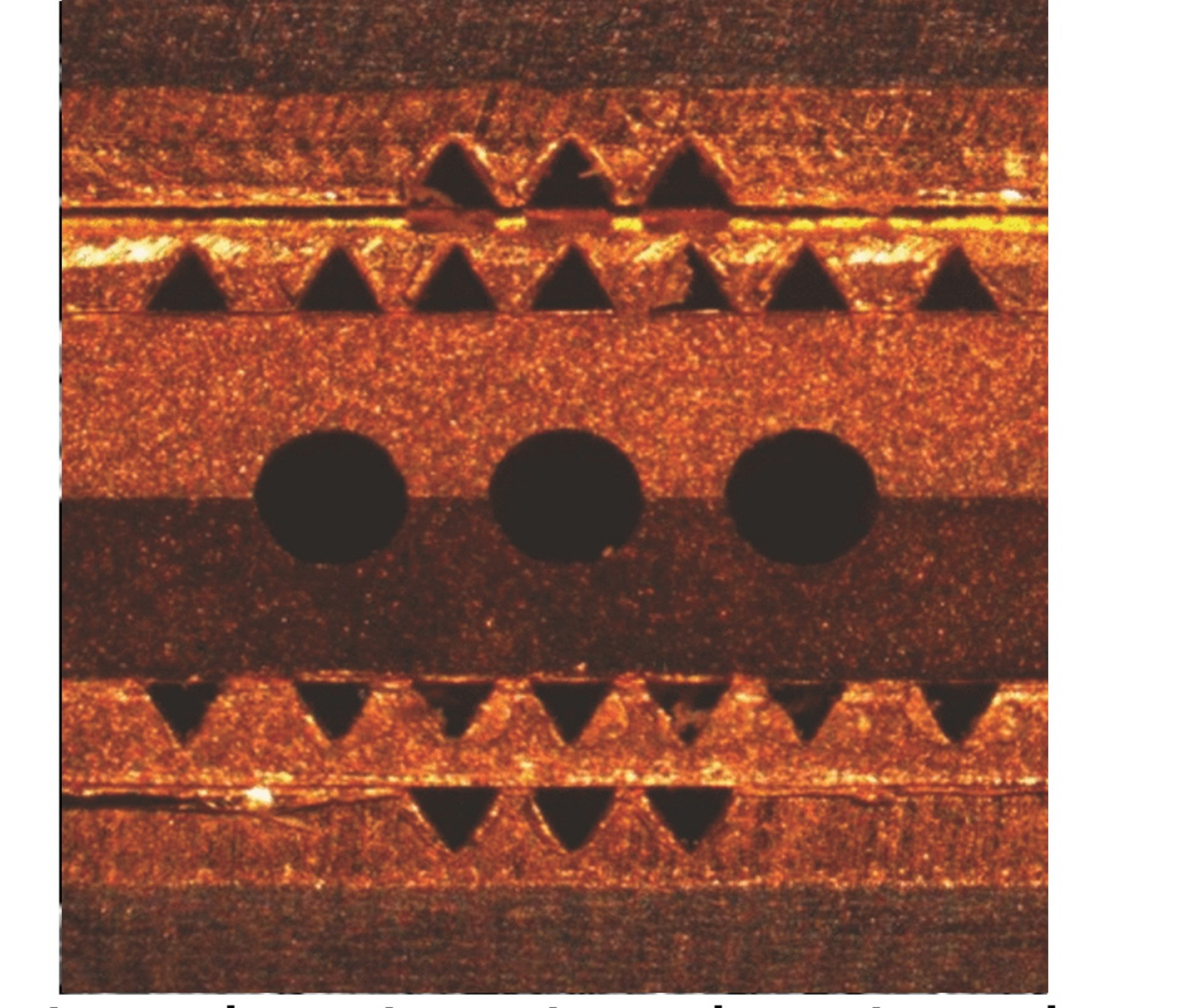
-1.5
-1.0
-0.5
0
0.5
1.0
1.5 mm

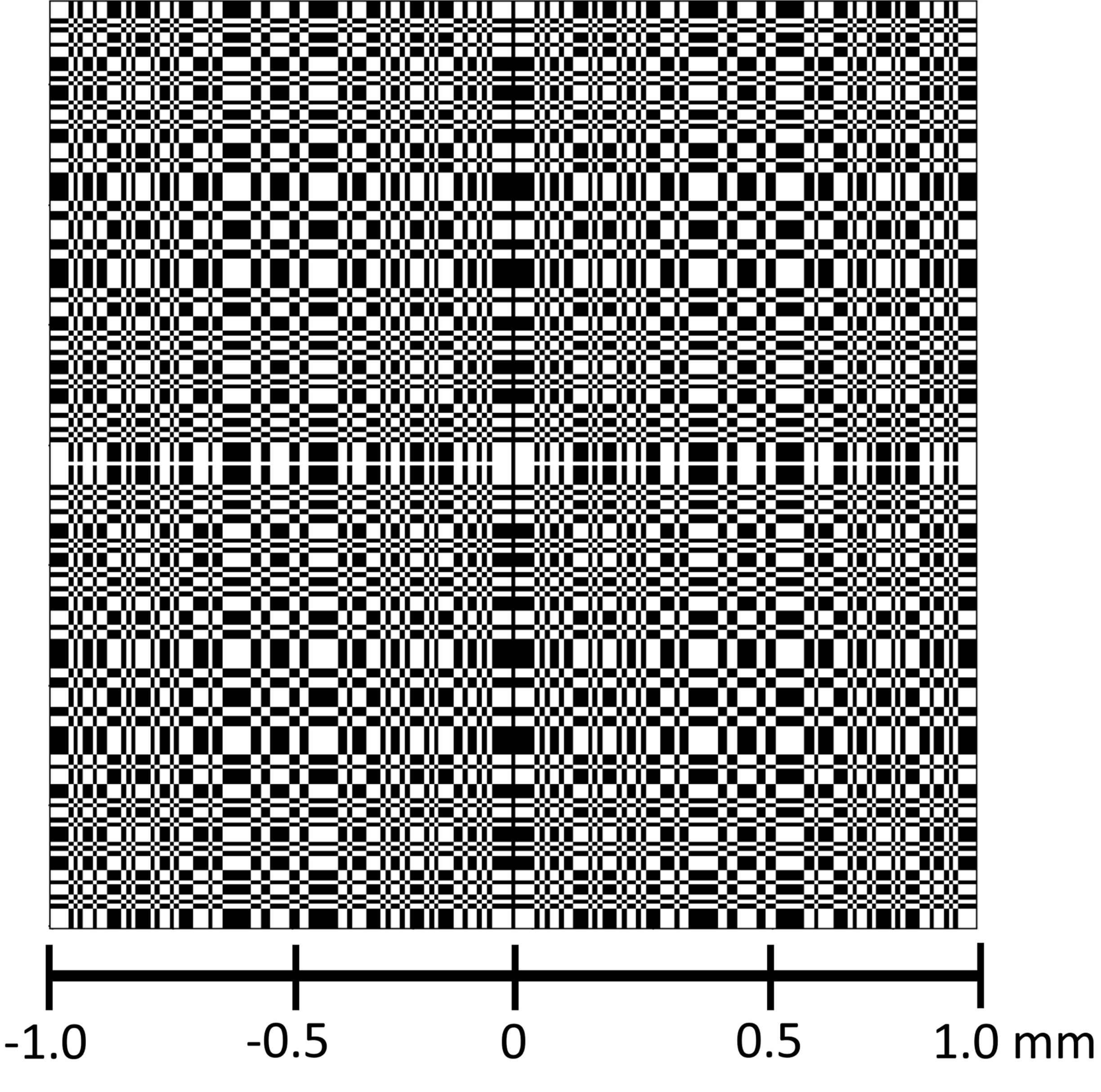
-1.0
-0.5
0
0.5
1.0 mm

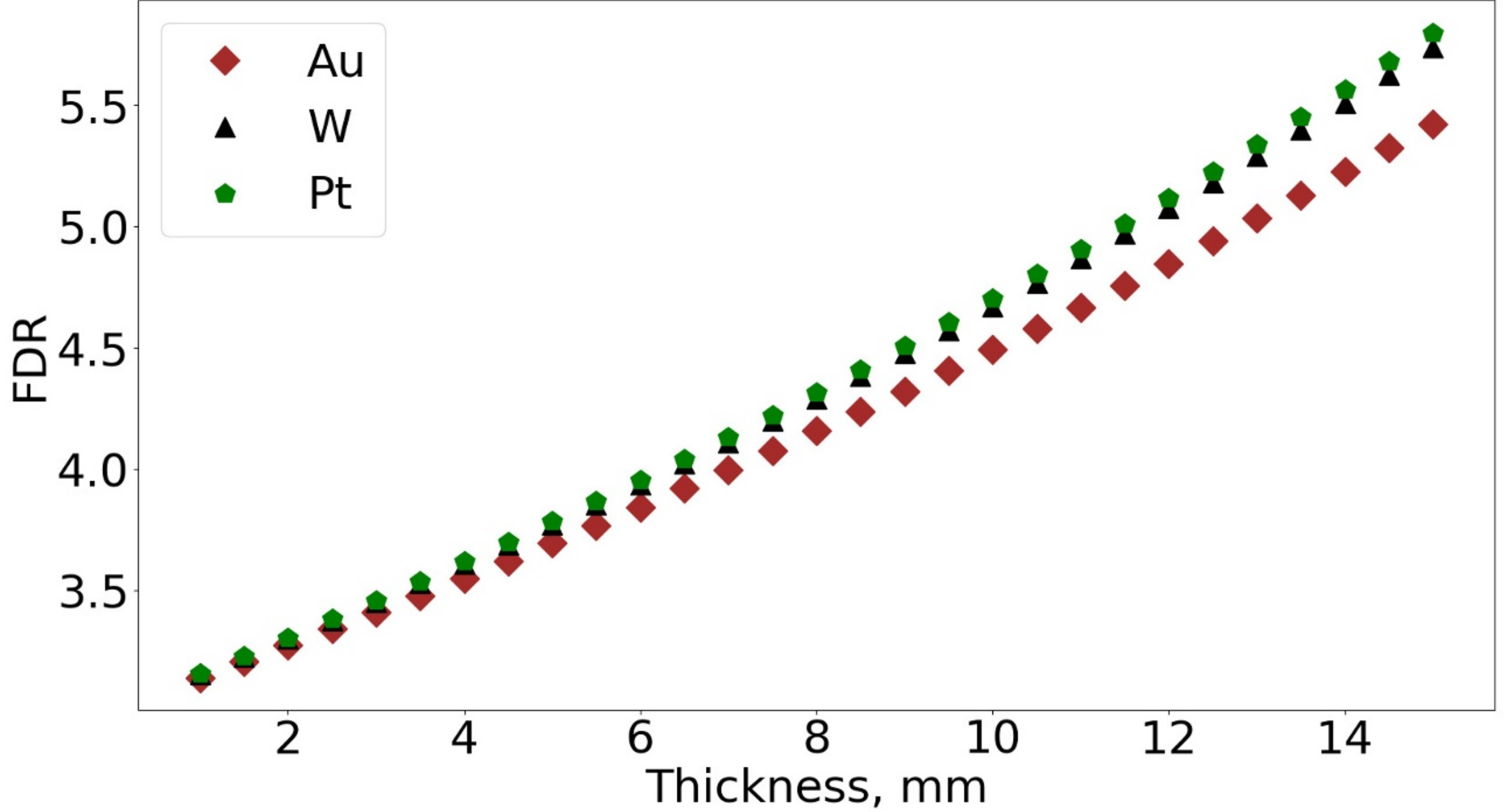
Au
W
Pt
FDR
5.5
5.0
4.5
4.0
3.5
2
4
6
8
10
12
14
Thickness, mm

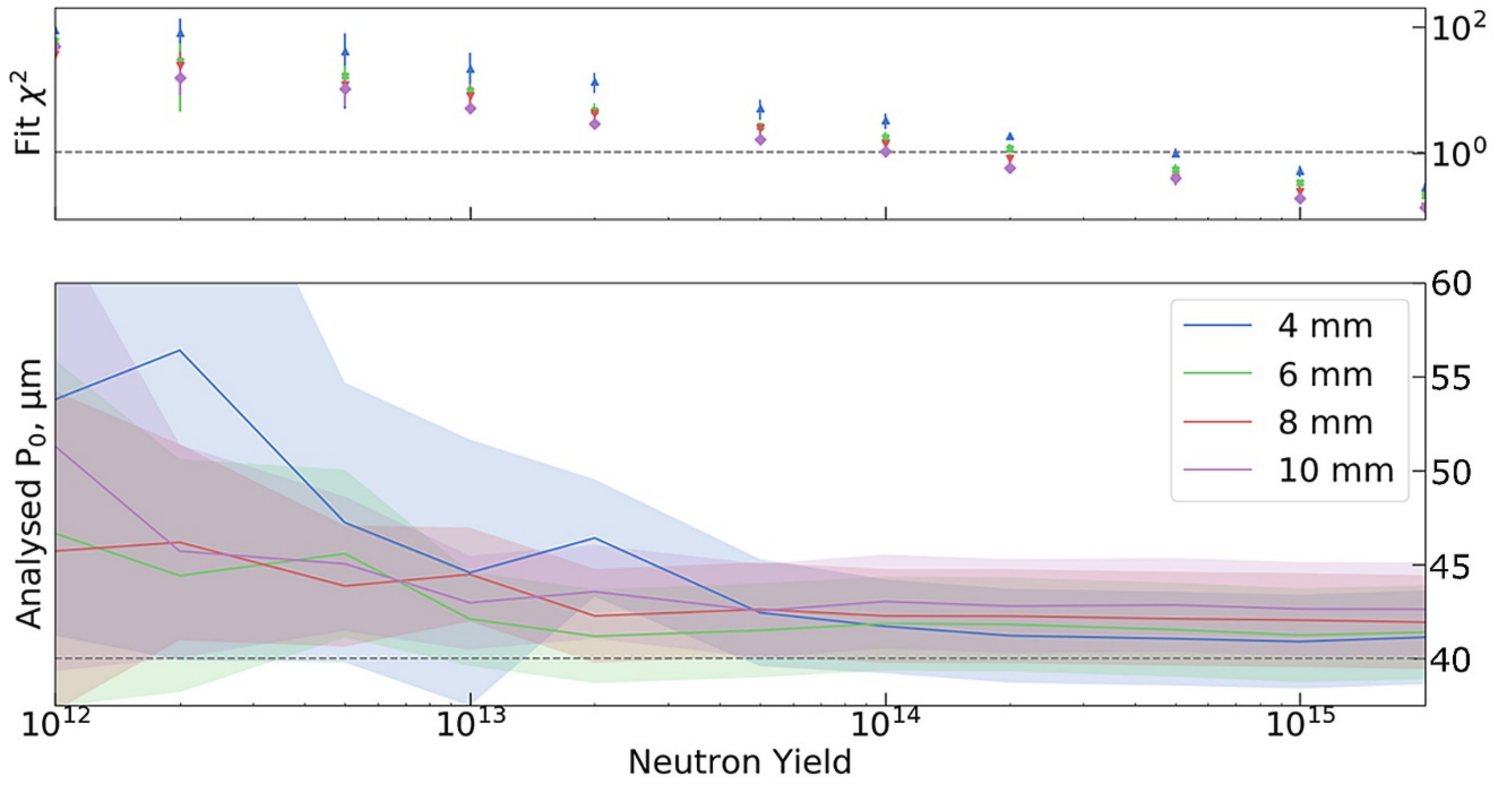
Fit χ^2
10^2
10^0
Analysed P_0, µm
60
55
50
45
40
4 mm
6 mm
8 mm
10 mm
10^{12}
10^{13}
10^{14}
10^{15}
Neutron Yield

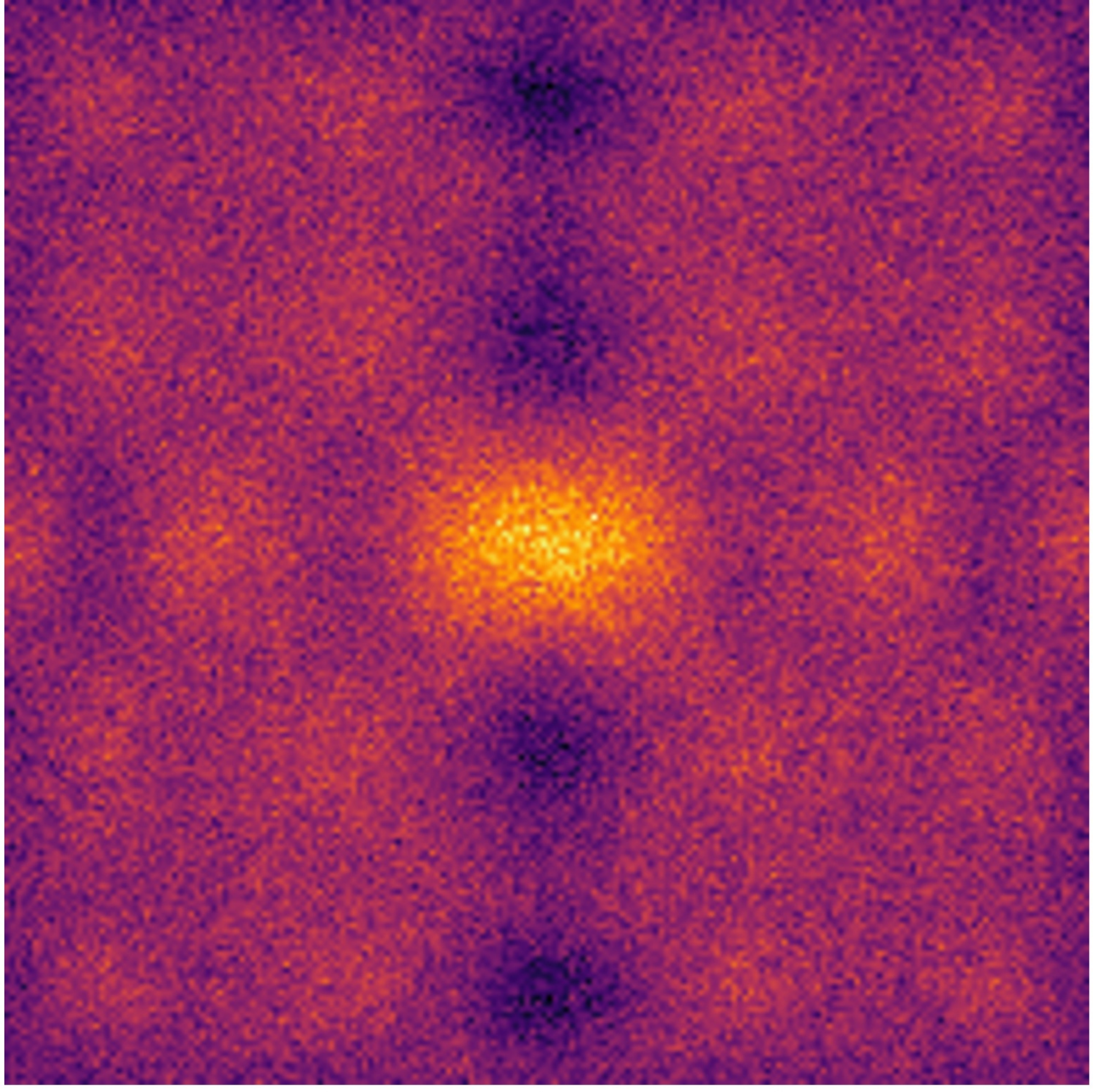
-20
-10
0
10
20 mm

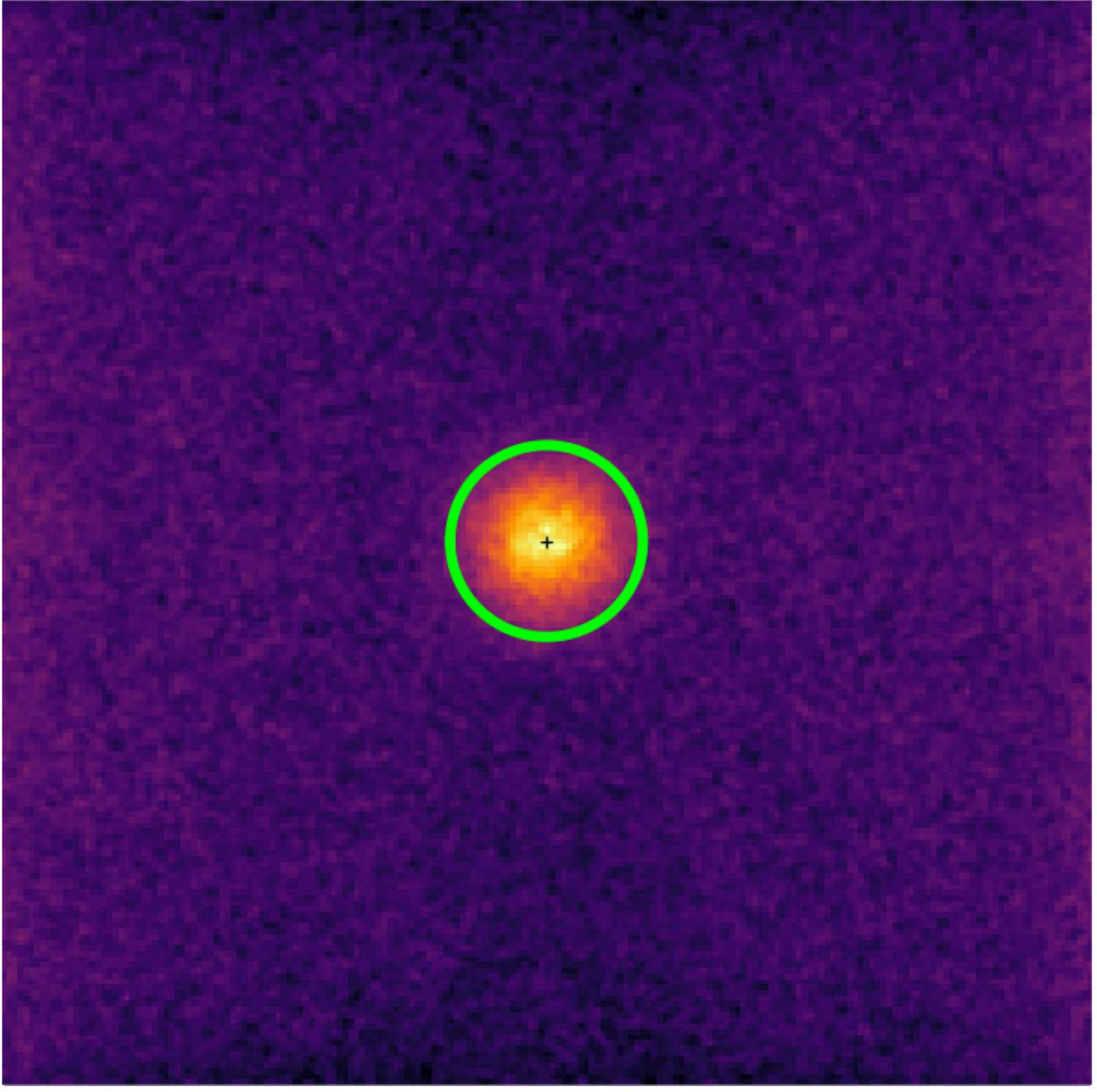
-20
-10
0
10
20 mm

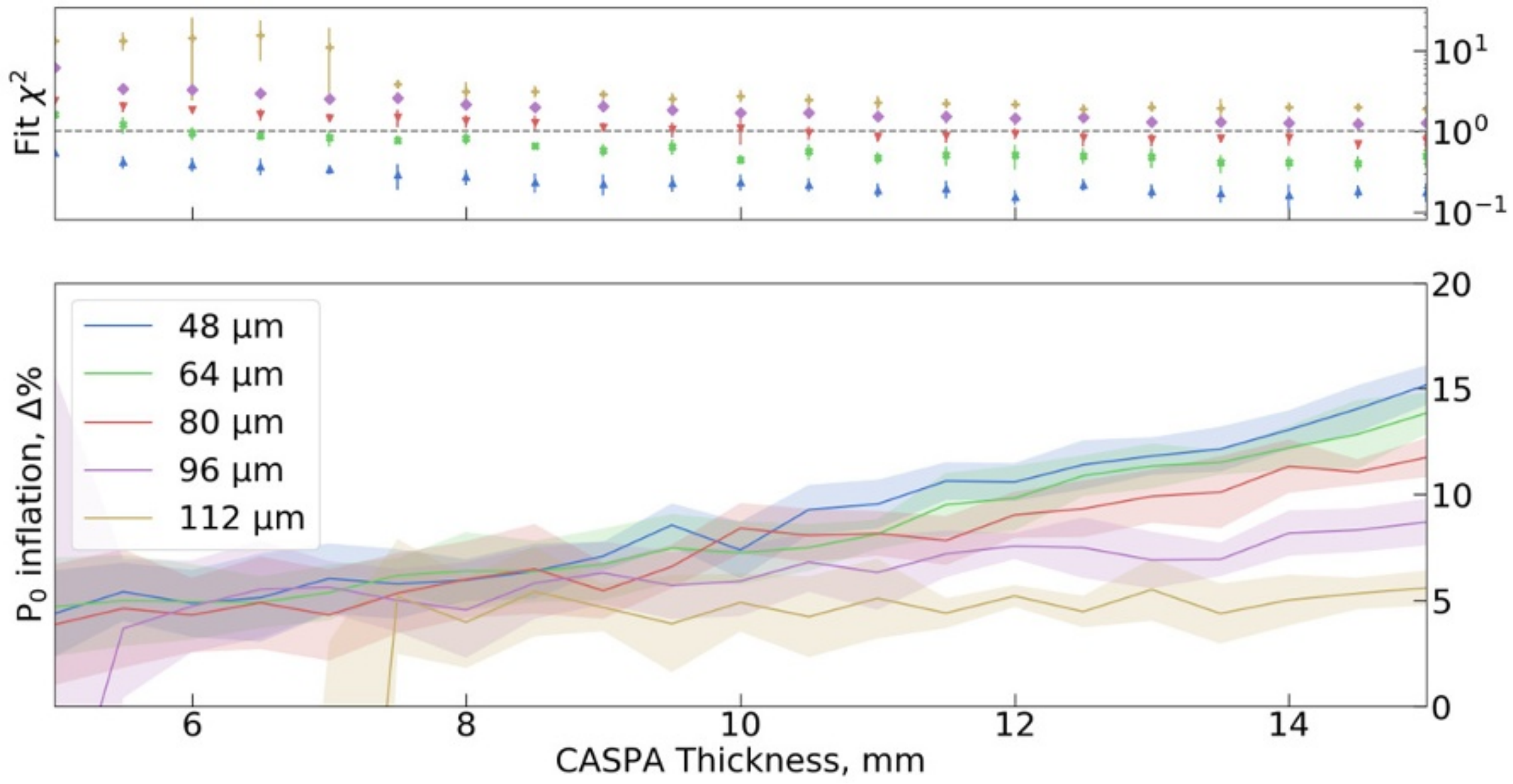
Fit χ^2
10^1
10^0
10^{-1}
P_0 inflation, Δ%
48 µm
64 µm
80 µm
96 µm
112 µm
20
15
10
5
0
6
8
10
12
14
CASPA Thickness, mm

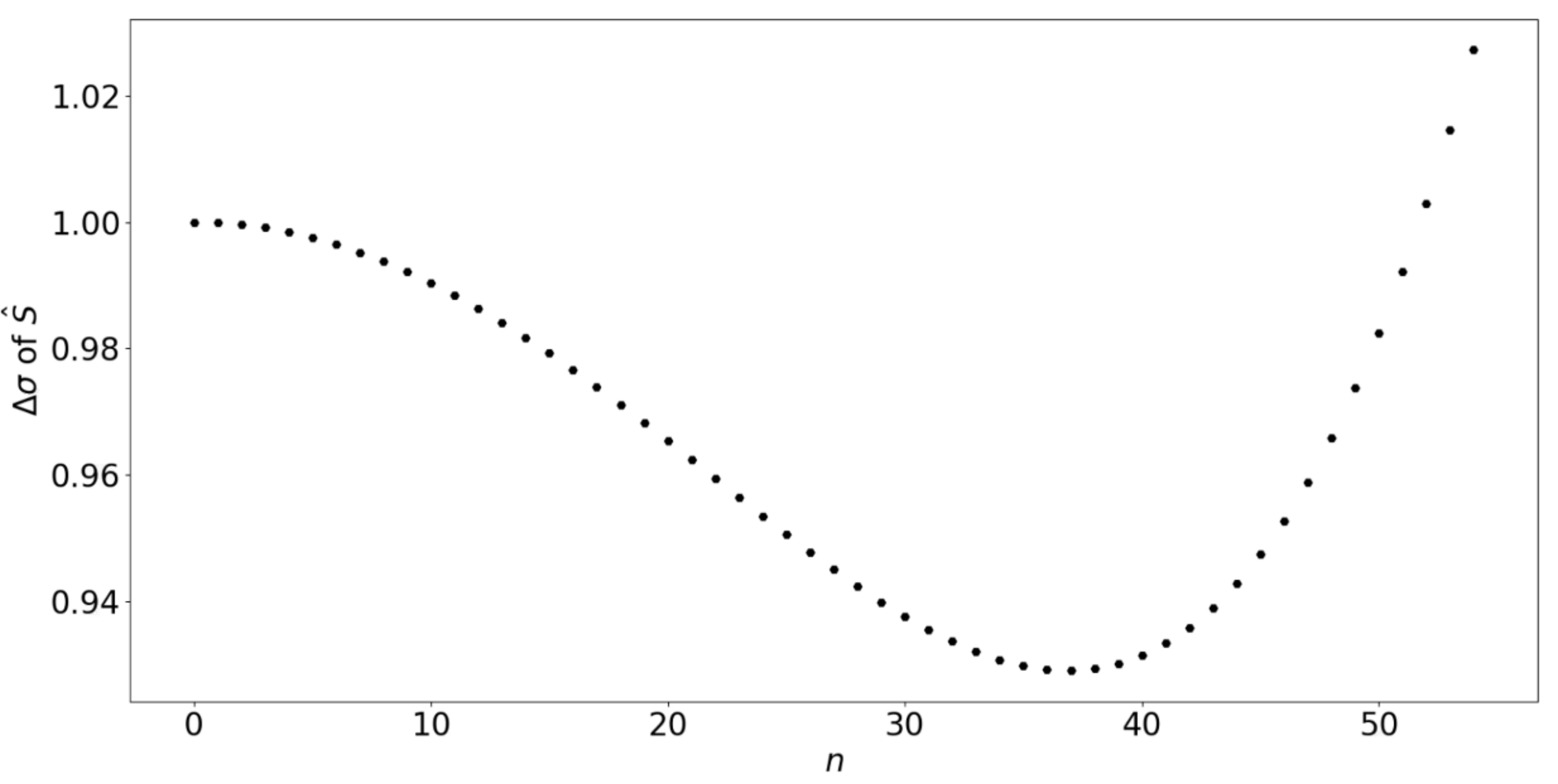
1.02
1.00
0.98
0.96
0.94
$\Delta\sigma$ of $\hat{S}$
0
10
20
30
40
50
n

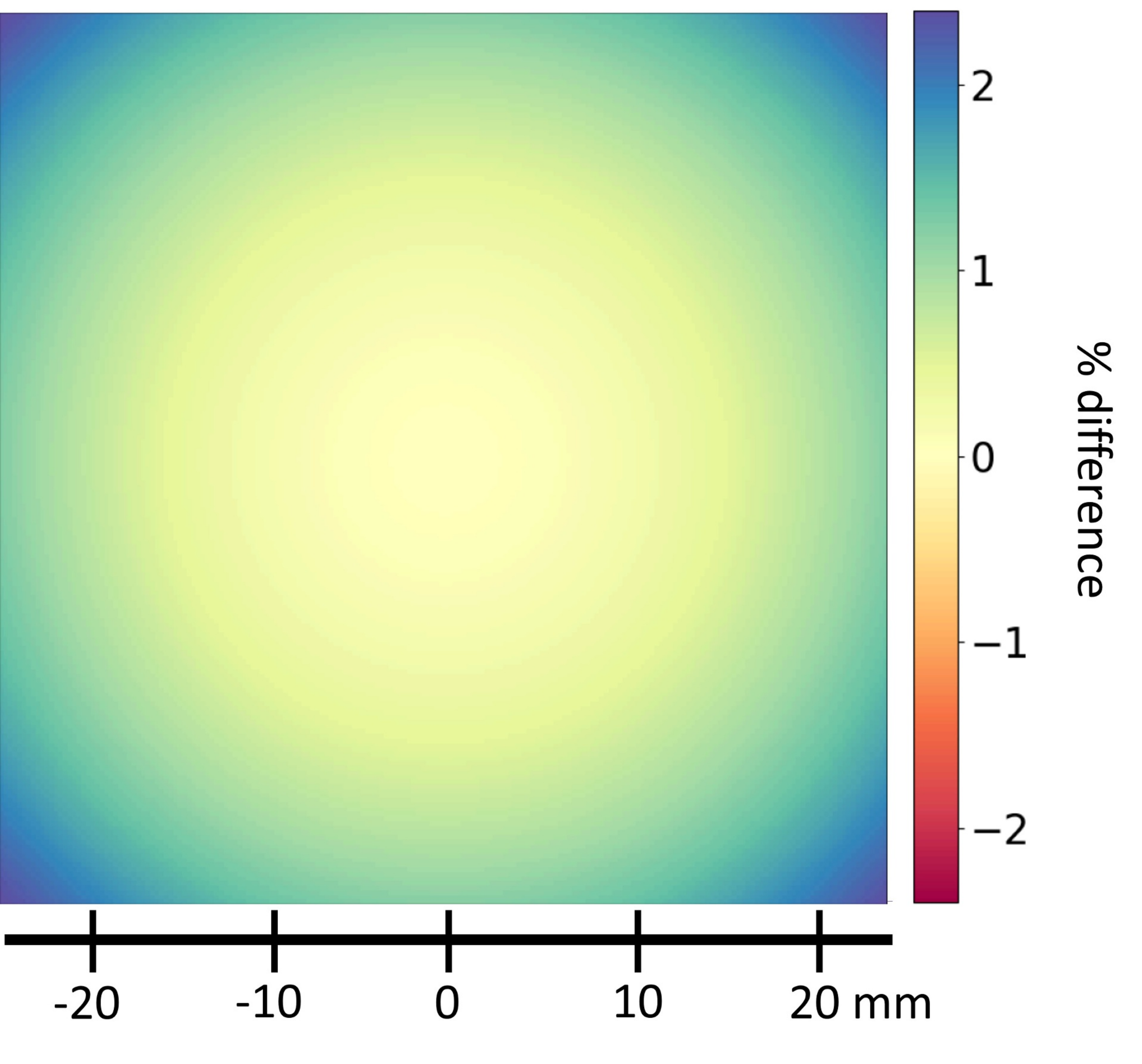
2
1
0
−1
−2
% difference
-20
-10
0
10
20 mm

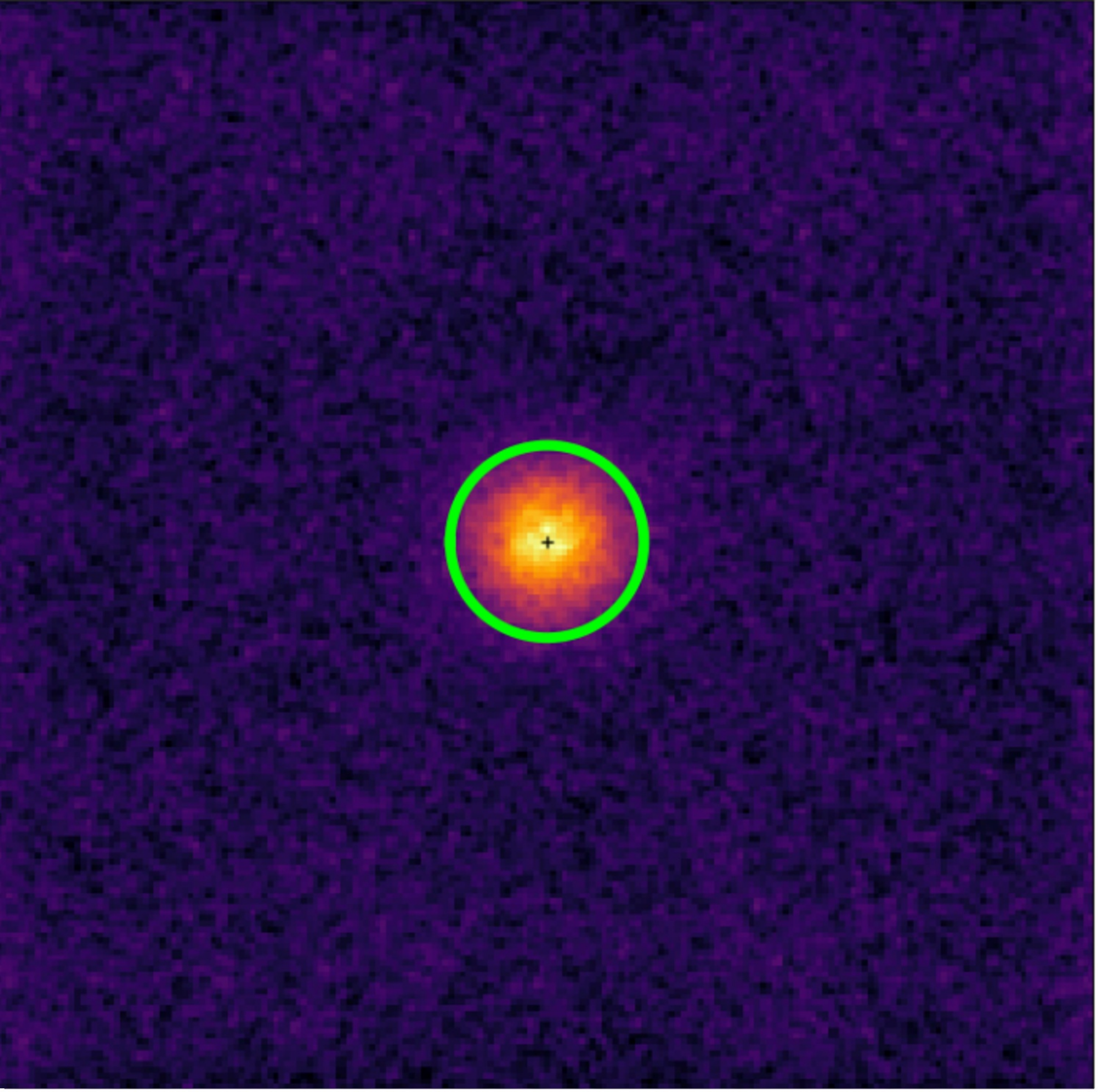
-20
-10
0
10
20 mm

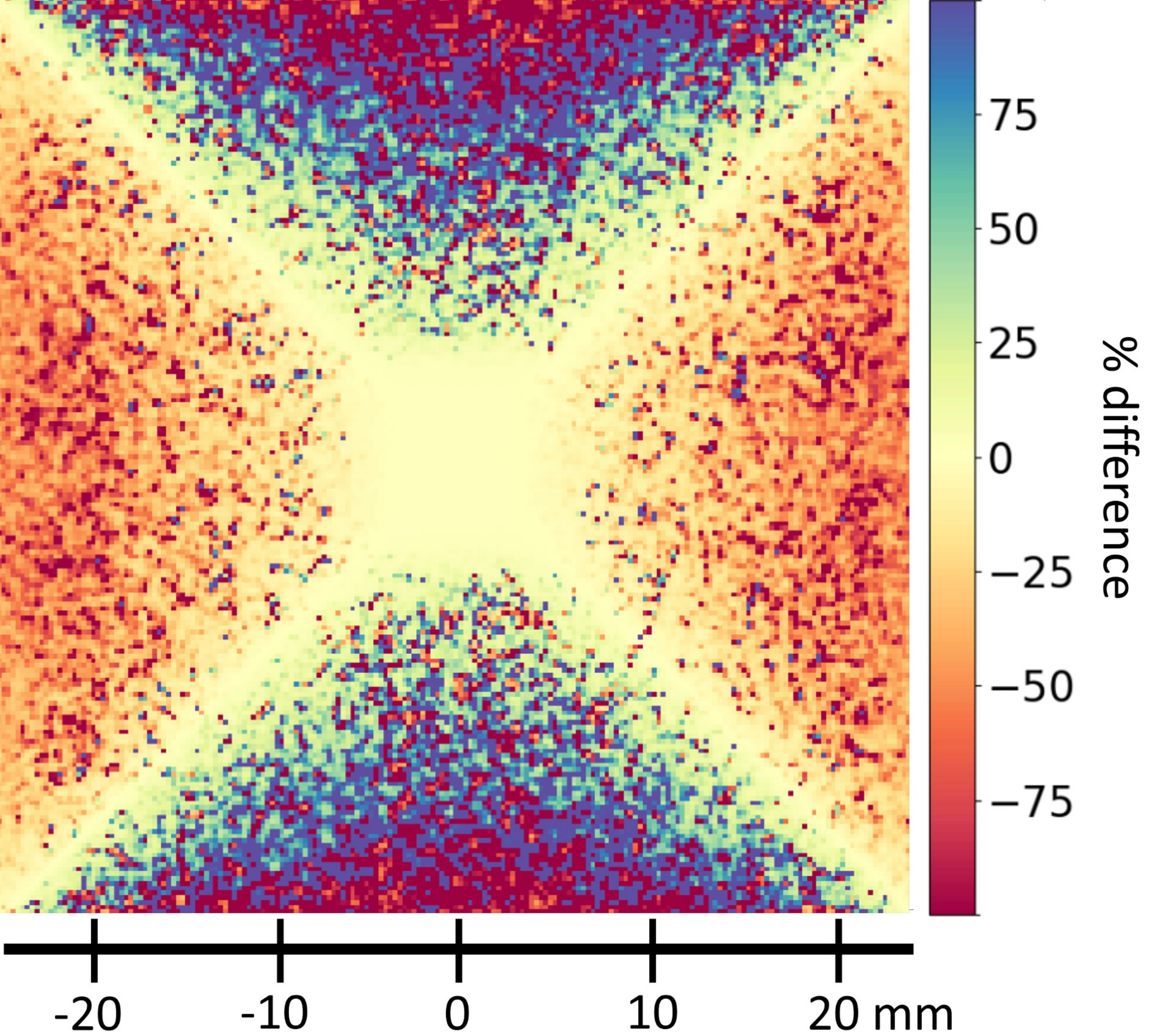
75
50
25
0
−25
−50
−75
% difference
-20
-10
0
10
20 mm

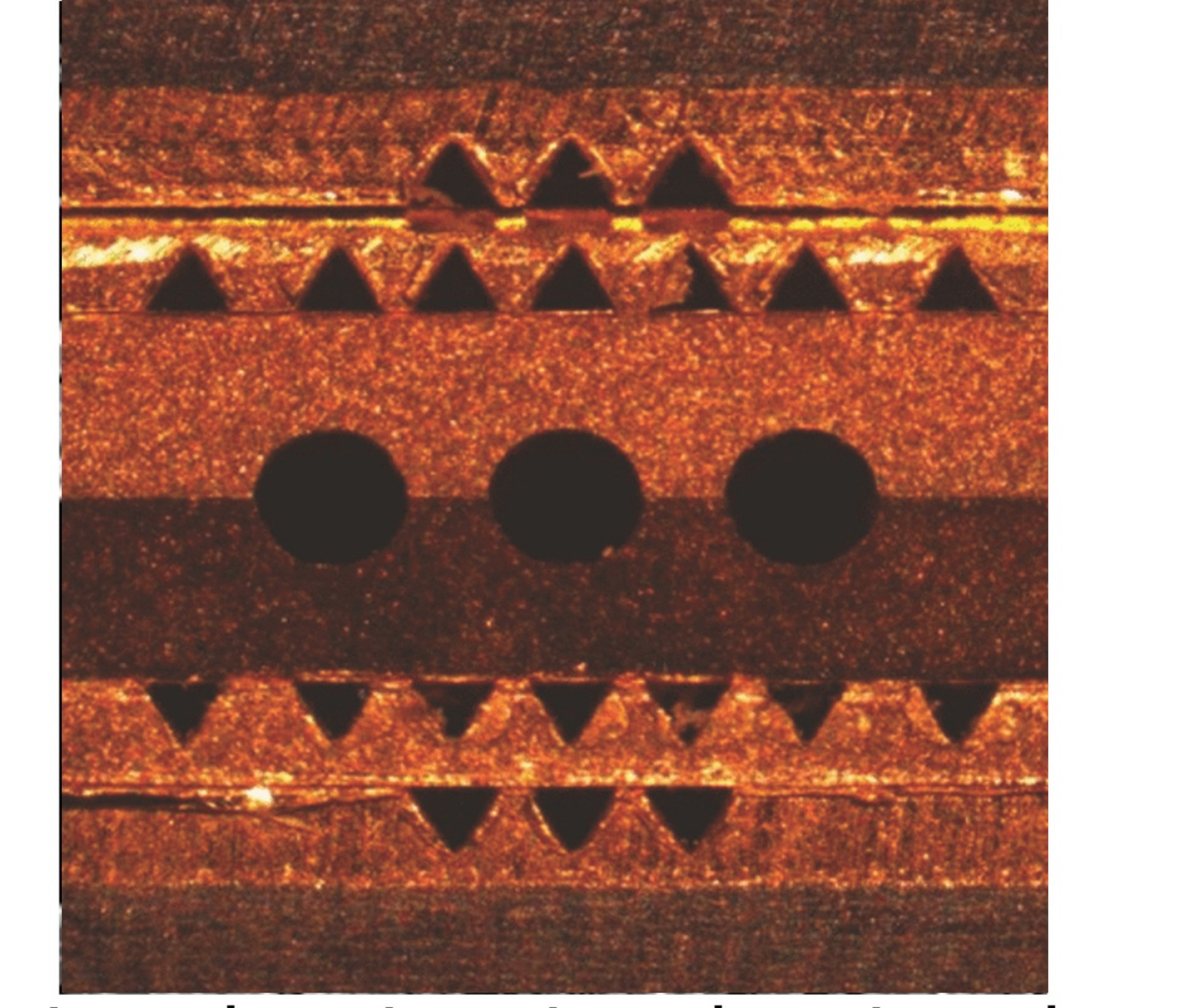
-1.5
-1.0
-0.5
0
0.5
1.0
1.5 mm

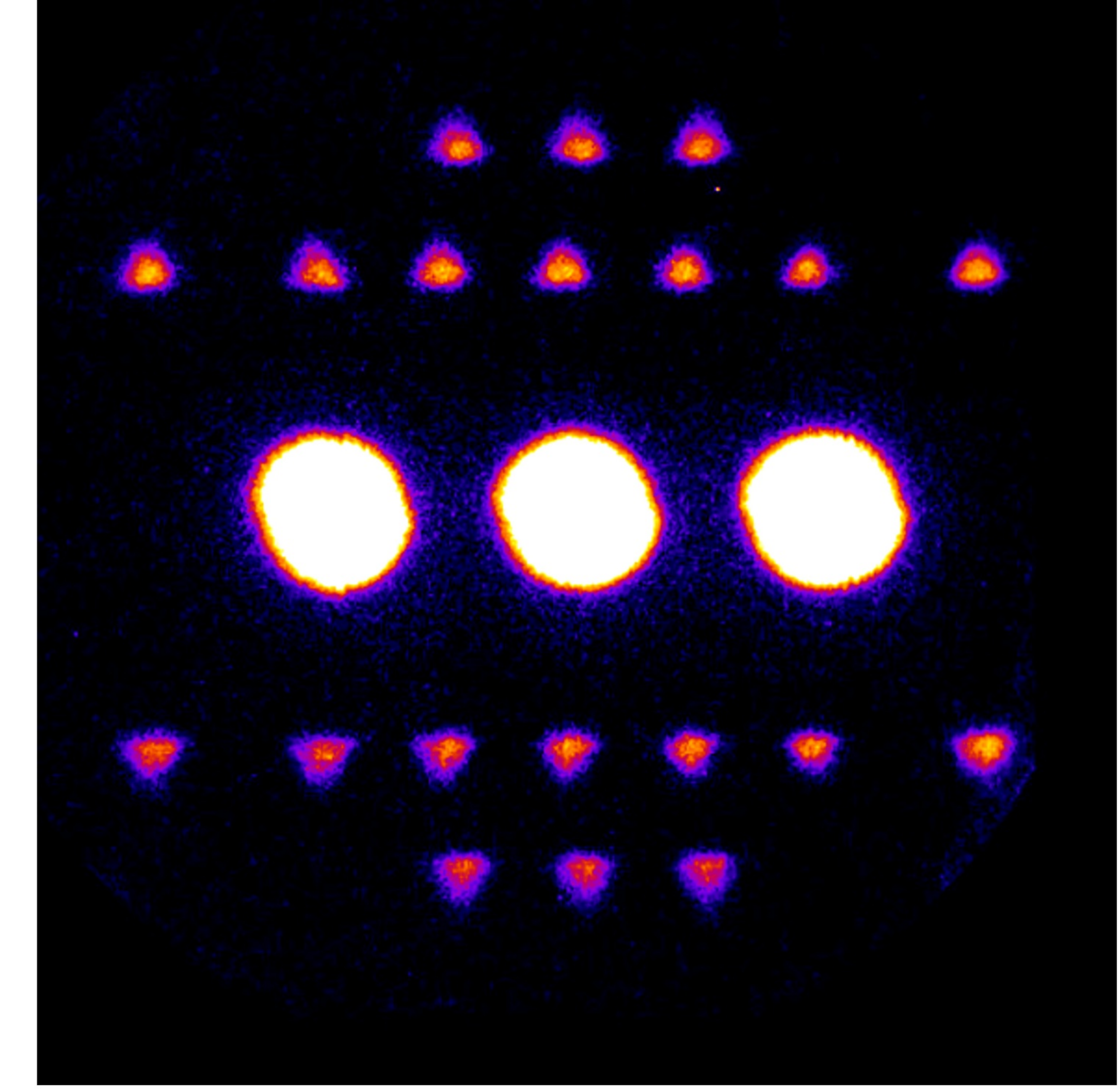
-60
-40
-20
0
20
40
60 mm

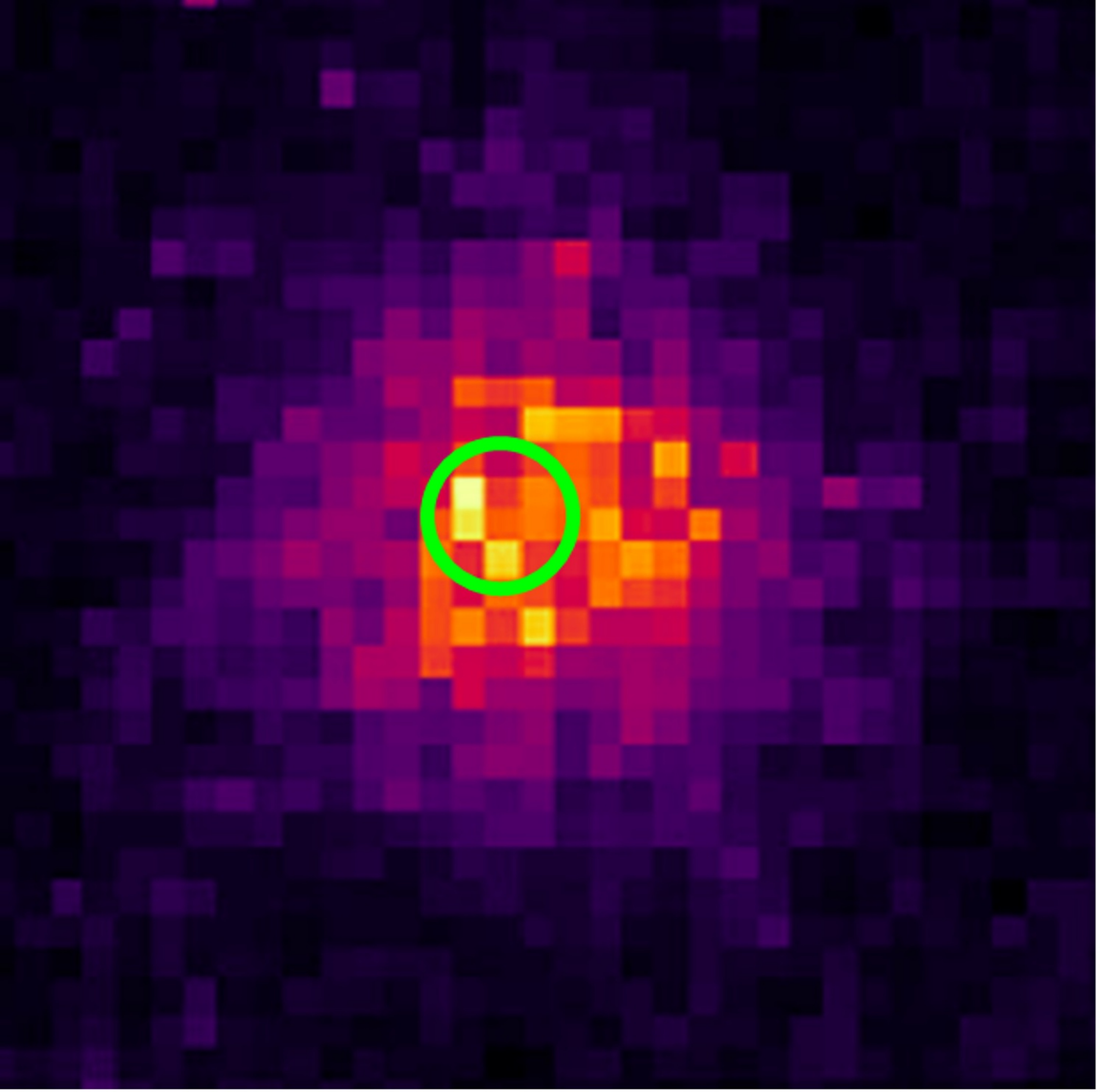
-150
-100
-50
0
50
100
150 µm

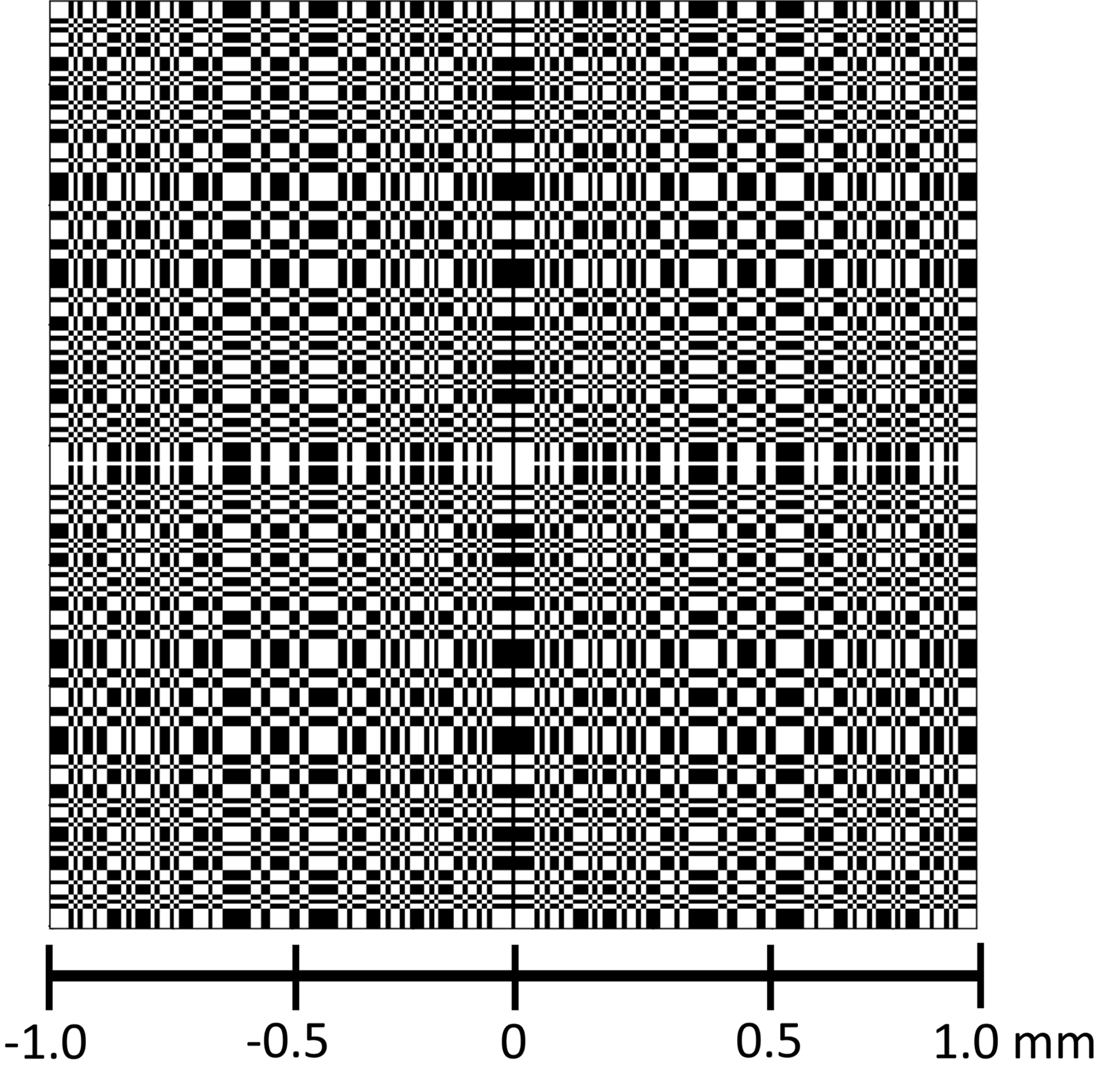
-1.0
-0.5
0
0.5
1.0 mm

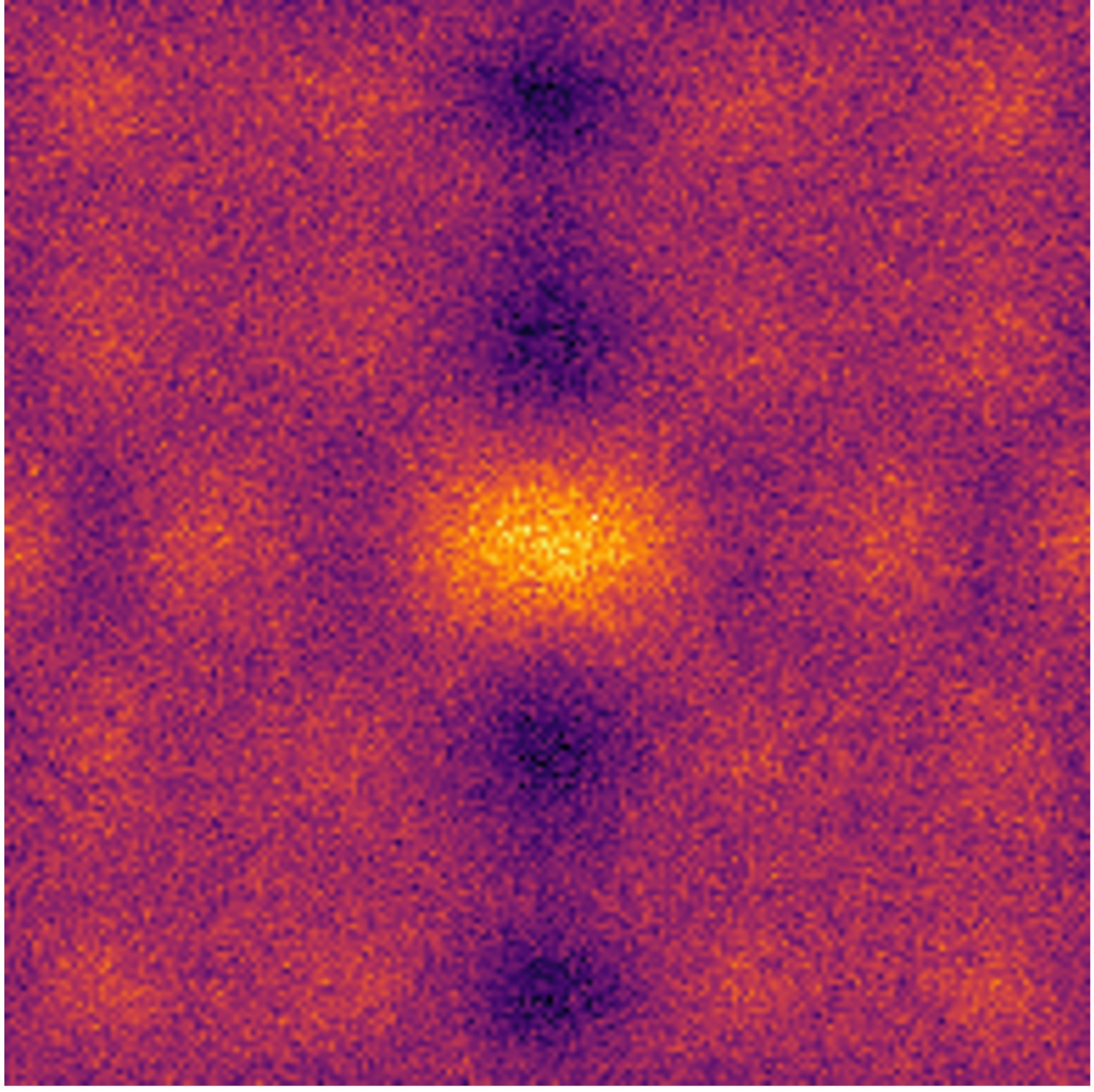
-20
-10
0
10
20 mm

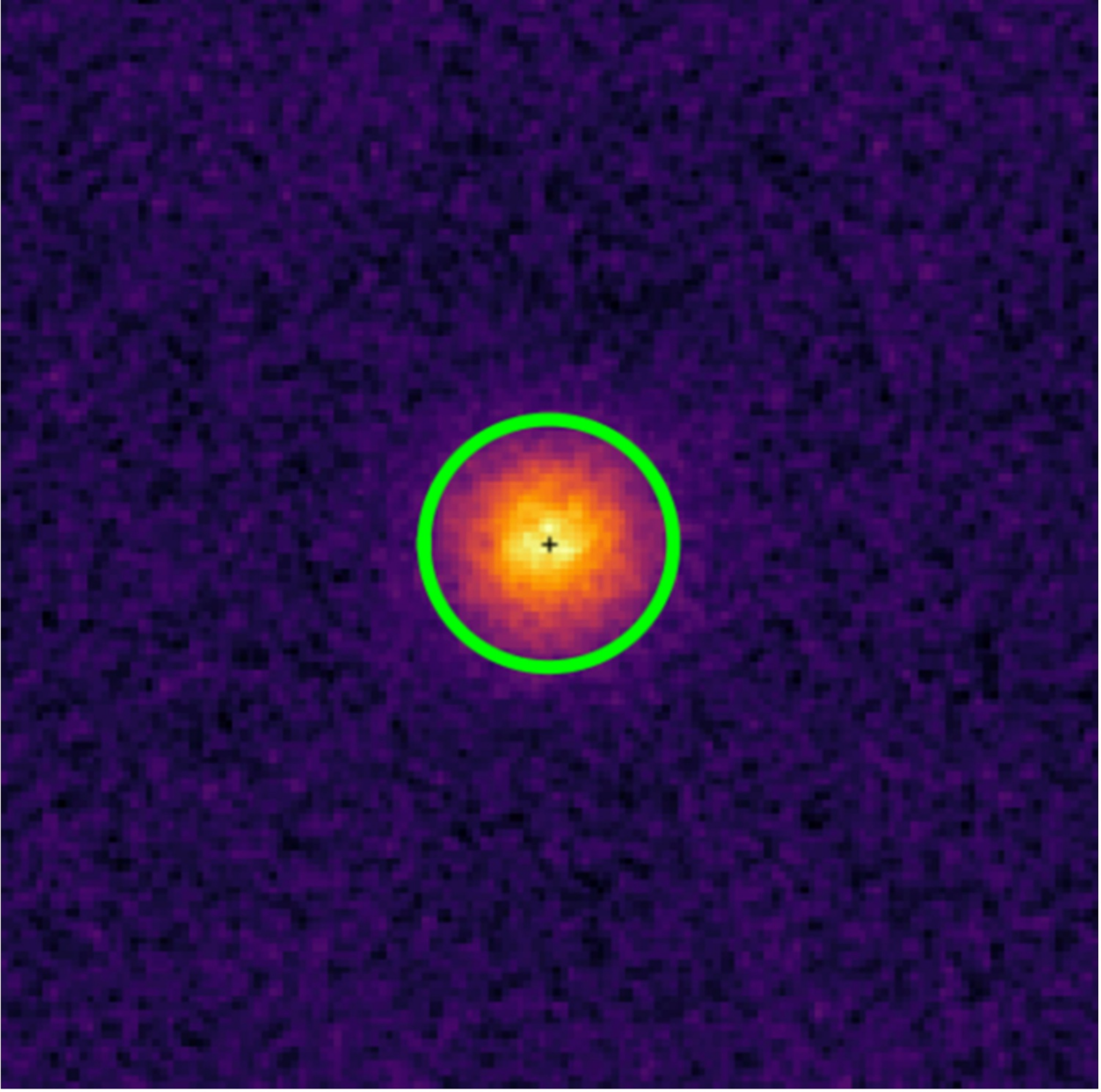
-150
-100
-50
0
50
100
150 µm